Mieap forms membraneless organelles to compartmentalize and facilitate cardiolipin metabolism

Naoki Ikari, Katsuko Honjo, Yoko Sagami, Yasuyuki Nakamura, and Hirofumi Arakawa*

Division of Cancer Biology, National Cancer Center Research Institute
5-1-1 Tsukiji, Chuo-ku, Tokyo 104-0045, Japan

*Correspondence should be addressed to:
Hirofumi Arakawa, M.D., Ph.D.
Division of Cancer Biology
National Cancer Center Research Institute
5-1-1 Tsukiji, Chuo-ku, Tokyo 104-0045, JAPAN
Tel: +81-3-3547-5273, Fax: +81-3-3546-1369
E-mail: harakawa@ncc.go.jp

Abstract

Biomolecular condensates function as membraneless organelles that compartmentalize and facilitate efficient biological reactions. They are formed by proteins with intrinsically disordered regions (IDRs) via liquid–liquid phase separation. Mieap/SPATA18, a p53-inducible protein, participates in suppression of colorectal tumors by promoting mitochondrial quality control. However, the regulatory mechanism involved remains unclear. Here, we report that Mieap is an IDR-containing protein that drives formation of biomolecular condensates in mitochondria. Mieap biomolecular condensates specifically phase separate the mitochondrial phospholipid, cardiolipin. Lipidomic analysis of cardiolipin suggests that Mieap promotes enzymatic reactions involved in cardiolipin metabolism, including biosynthesis and remodeling. Accordingly, four cardiolipin biosynthetic enzymes, TAMM41, PGS1, PTPMT1, and CRLS1, and two remodeling enzymes, PLA2G6 and TAZ, are phase-separated by Mieap biomolecular condensates. Mieap-deficient mice exhibit altered crista structure in mitochondria of various tissues, including brown fat, and tend to become obese. These results suggest that Mieap drives formation of membraneless organelles to compartmentalize and promote cardiolipin metabolism at the inner mitochondrial membrane, thus potentially contributing to mitochondrial quality control.

Introduction

Biomolecular condensates (BCs) in cells are also known as liquid droplets because of their liquid-like nature. BCs are composed of proteins, nucleic acids, and other macromolecular components[1-3], and they are formed by proteins with intrinsically disordered regions (IDRs) via liquid–liquid phase separation (LLPS). Importantly, BCs function as membraneless organelles (MLOs) that compartmentalize and facilitate cellular biological reactions. BCs are not surrounded by lipid bilayers, which enables facile exchange of reactants and products with their surroundings, expediting biological reactions in cells. Furthermore, theoretically, BCs are able to appear and disappear within a cell in response to cellular stress and/or subcellular circumstances, exhibiting spatiotemporally dynamic properties. On the basis of these features, the concept of MLOs is fundamentally different from the long-standing concept of membrane-bound organelles, such as nuclei, lysosomes, mitochondria, and endoplasmic reticulum, stable structures that segregate biomolecules and biological reactions using lipid bilayer membranes. Multiple MLOs may exist within a cell, possibly regulating cellular biological reactions and activities, including transcriptional regulation[4], signal transduction[5,6], immunity[7], centrosome activity[8], and mitosis[9]. This list is rapidly growing.

Metabolic reactions are believed to be highly organized through spatiotemporal clustering and compartmentalization of sequential enzymes and substrates/intermediates at subcellular sites, which maximizes efficiency of linked reactions[10]. Without this mechanism, small, toxic intermediates, derived from metabolic reactions, rapidly diffuse throughout the cytoplasm. Thus, the concept of subcellular compartmentalization of metabolic reactions has been anticipated for a long time. It was initially conceived as a "metabolon," a structural-functional complex of sequential metabolic enzymes and substrates/intermediates[11]. The "metabolon" concept predicted that sequential enzymes and cellular structural elements form a supramolecular complex for metabolic reactions. In fact, many studies have demonstrated that enzyme clustering *in vivo* may facilitate sequential enzymatic metabolic reactions[12-15]. Among them, "purinosomes" involved in purine metabolism, were the first demonstration of enzyme clustering, revealed by live-cell imaging of six sequential enzymes for *de novo* purine synthesis[16]. Although MLOs that compartmentalize and expedite metabolic reactions in cells could address regulatory mechanisms for sequential metabolic reactions, there has been no clear evidence for metabolic MLOs until now.

So far, two studies demonstrated the roles and regulatory mechanisms of MLOs (BCs) in enzymatic reactions. Kim and Tsang et al. reported that modifications of IDRs of scaffold proteins control architecture and enzymatic activity within MLOs[17]. In terms of MLOs involved in RNA processing, utilizing the IDRs of FMRP and CAPRIN1, they demonstrated that RNA adenylation and translation are inversely controlled by phosphorylation patterns of the IDRs, which change condensate architecture and enzymatic activity. Peeples and Rosen reported that enzymatic reactions in condensates are accelerated by both mass action and change in substrate K_M[18]. Utilizing a synthetic system where the SUMOylation enzyme cascade is recruited into engineered condensates, they demonstrated that reaction rates can be increased up to 36-fold in condensates compared to the surrounding bulk, and that condensates can modulate reaction rates by not only concentrating

enzymes and substrates, but also by physically organizing them. These results strongly suggest the importance of MLOs in regulation of sequential enzymatic reactions in metabolism.

Cardiolipin (CL) is an important phospholipid for the following reasons. [1] It is a phospholipid dimer, with two phosphate residues and four fatty acyl chains[19]. [2] Because of this unique structure, it forms a cone shape, contributing to curvature of the lipid membrane and to maintenance of mitochondrial cristae[20]. [3] CL is the only phospholipid that is specific to mitochondria and is mainly located at the inner mitochondrial membrane and contact sites[20]. [4] CL interacts with many mitochondrial membrane proteins, including electron transport chain complexes involved in oxidative phosphorylation, and the ADP/ATP carrier. Interaction with CL promotes activity of these proteins[20]. [5] CL stabilizes the structural assembly and activity of respiratory super-complexes at the inner mitochondrial membrane[21]. [6] It interacts with cytochrome *c* at the outer surface of the inner mitochondrial membrane, which supports cellular viability by maintaining stable respiratory ATP production and inducing apoptosis, respectively[21]. Therefore, control of CL quality and quantity appears to be important for various mitochondrial functions.

CL metabolic reactions comprise two processes, CL biosynthesis and remodeling. CL metabolic enzymes are characterized and studied in yeast cells, and human orthologs of yeast enzymes have been reported[22]. In brief, phosphatidic acid (PA) is synthesized in the endoplasmic reticulum and subsequently transported by PRELI (yeast Ups1) via the outer mitochondrial membrane to the inner mitochondrial membrane, as the substrate of CL metabolism[22,23]. In CL biosynthesis, PA is converted to nascent CL on the matrix face of the inner mitochondrial membrane through sequential enzymatic reactions that produce three intermediates, CDP-diacylglycerol (CDP-DG), phosphatidylglycerophosphate (PGP), and phosphatidylglycerol (PG). These reactions are catalyzed by a series of four enzymes, TAMM41 (yeast Tam41), PGS1 (yeast Pgs1), PTPMT1 (yeast Gep4), and CRLS1 (yeast Crd1) (20,22). The final step of CL metabolic reactions is remodeling of nascent CL to mature CL, which is catalyzed by PLA2G6/iPLA2β (yeast Cld1) and TAZ (yeast Taz1) [22,24]. These cascading enzymatic reactions are thought to be continuously executed at the inner mitochondrial membrane. However, how these enzymatic reactions can be continuous and/or how CL metabolic reactions are regulated remain unknown.

Altered CL metabolism and/or deterioration of CL quality and quantity due to CL metabolic enzyme deficiency causes various mitochondrial dysfunctions in eukaryotes ranging from yeast to mammals[22,25]. Specifically, Barth syndrome is a human disease caused by mutations in the TAZ gene encoding tafazzin, the enzyme responsible for CL remodeling[26]. Clinical symptoms of Barth syndrome patients include cardiomyopathy, skeletal muscle weakness, neutropenia, and growth retardation. Barth syndrome models, including lymphoblasts and induced pluripotent stem cells derived from patients, exhibit abnormal crista structures, decreased respiration activity, and increased reactive oxygen species (ROS) generation in mitochondria[27,28]. This implies that substantial regulation of CL metabolic reactions is required to maintain mitochondrial functions and to prevent diseases. However, the regulatory mechanism for CL metabolic reactions is unknown.

Mitochondria-eating protein (Mieap, also denominated SPATA18) was originally identified as

a p53-inducible protein. Its mRNA expression is directly regulated by the tumor suppressor, p53, in response to various cellular stresses, including DNA damage[29]. Mieap expression is lost in nearly 50% of human cancer cell lines due to promoter methylation. Mieap-deficient LS174T colorectal cancer cells generate higher levels of mitochondrial ROS and synthesize less ATP. Mitochondrial ROS in Mieap-deficient colorectal cancer and gastric cancer cells enhances migration and invasiveness of cancer cells under hypoxic conditions[30,31]. Mieap deficiency promotes intestinal tumors in $Apc^{Min/+}$ mice[32]. Tumors in Mieap-deficient ApcMin/+ mice reveal abnormal mitochondrial morphology, such as large size, round shape, and disordered cristae. Mieap expression is defective in thyroid oncocytic cell tumors, which accumulate abnormal mitochondria in tumor cells[33]. Mieap-regulated mitochondrial quality control is inactivated in tumor tissues of nearly 70% of colorectal cancer and 25% of breast cancer patients[30,34]. These observations suggest that Mieap suppresses tumors via mitochondrial quality control. However, the mechanism underlying regulation of mitochondrial quality control by Mieap remains unclear.

Here, we report that Mieap is an IDR-containing protein that drives BC formation in mitochondria. Mieap BCs phase separate the mitochondrial phospholipid, CL. The present findings suggest that Mieap BCs function as MLOs that compartmentalize and promote CL synthesis and remodeling reactions at the inner mitochondrial membrane, leading to stabilization of oxidative phosphorylation and suppression of mitochondrial ROS generation. Thus, we suggest that the Mieap-CL axis is the regulatory mechanism for efficient CL metabolic reactions and/or CL quality and quantity control, forming MLOs that govern mitochondrial quality control by regulating CL synthesis and remodeling. Dysregulation of this pathway leads to mitochondrial dysfunction due to CL alterations, causing a variety of diseases and/or pathologies, including cancer, obesity, and infertility.

Results

Mieap forms biomolecular condensates in mitochondria

Mieap has been reported to form vacuole-like structures, designated as Mieap-induced vacuoles (MIVs), which were thought to directly assimilate mitochondria[35] in a non-canonical type of mitophagy. To examine MIV formation and "non-canonical mitophagy" in live cells, we constructed a recombinant adenovirus to express EGFP-tagged Mieap and observed cells expressing EGFP-Mieap using confocal live-cell imaging. Multiple spherical green signals (EGFP-Mieap) appeared around the red mitochondrial signals (MitoTracker Red) (Supplementary Fig. 1a and Movie 1). These oval green signals fused, enlarged, and eventually coalesced into a few large, spherical structures. In contrast, red mitochondrial signal intensity decreased during this process. These results were consistent with our previous interpretation of non-canonical mitophagy; however, they also indicated that the structures formed by EGFP-Mieap are not the ring-shaped formations, previously reported using immunofluorescence (IF) [35].

Thus, we repeated the IF experiment on structures comprising EGFP-Mieap. EGFP-Mieap reproducibly formed green condensates, while antibodies (anti-Mieap antibody and anti-GFP antibody) produced ring-shaped staining around the green condensates (Supplementary Fig. 1b). Thus, we suspected that antibodies are unable to permeabilize EGFP-Mieap condensates.

We performed additional IF using anti-FLAG antibody for the MIV structures, which comprise N-FLAG-Mieap (N-terminal FLAG-tagged Mieap protein) and C-FLAG-Mieap (C-terminal FLAG-tagged Mieap protein). Ring-shaped staining was observed with N-FLAG-Mieap, but not C-FLAG-Mieap (Supplementary Fig. 1c), suggesting that Mieap may be positioned with its N-terminal domain facing outward at the surface of the condensates.

Using transmission electron microscopy (TEM), MIV structures appeared to consist of two phases: a dominant electron-dense phase that stained strongly with OsO_4, and an OsO_4-negative, electron-lucent minor phase (Supplementary Fig. 1d). In immunoelectron microscopy (IEM) analysis with anti-Mieap antibody, gold colloid staining indicated that Mieap protein was distributed over the major electron-dense phase (Supplementary Fig. 1e). Thus, both fluorescent tagging and antigen-antibody reactions confirmed that Mieap forms protein condensates, a process fundamentally distinct from "mitophagy." Mieap condensates exhibited spherical or oval shapes, fusion, and multi-phase structure consisting of two phases: a Mieap-containing phase and a Mieap-depleted phase (Supplementary Fig. 1d, e, and Movie 2). These characteristics, and their propensity to fuse, are not contradictory to a notion that Mieap condensates have liquid-like properties, suggesting that these structures are droplets[3]. Therefore, we designate Mieap-induced structures as Mieap BCs (Mi-BCs).

To clarify the spatial relationship between Mi-BCs and mitochondria, we performed live-cell imaging using cells co-expressing EGFP-Mieap and an outer mitochondrial membrane marker, mApple-TOMM20 (Supplementary Fig. 1f). In order to thoroughly evaluate the relationship between Mi-BCs and mitochondria, we captured images of nascent Mi-BCs before their enlargement. mApple-TOMM20 entirely surrounded small Mi-BCs, suggesting that Mieap forms condensates in

190 mitochondria (Fig. 1 a – c, and Supplementary Movie 3). Furthermore, our imaging analysis indicated
191 that even enlarged Mi-BCs may exist inside mitochondria (Fig. 1d).
192 Recently, a study reported that mitochondrial nucleoids exhibit droplet-like features[36].
193 Therefore, Mi-BCs are likely the second example of mitochondrial droplets. Considering the
194 efficiency and precision of imaging analyses, we examined the relatively enlarged Mi-BCs in the
195 following experiments.
196
197 **Mieap is an IDR-containing protein with potential to drive LLPS**
198 We performed *in silico* sequence analyses. Mieap orthologs were found in eukaryotes, but not in
199 bacteria, archaea, or viruses (Fig. 2a) [37]. Hence, the Mieap function evolved in eukaryotes. Moreover,
200 among eukaryotes, Mieap orthologs were found in metazoans, but not in fungi (Fig. 2a), suggesting
201 that Mieap is beneficial to multicellular organisms.
202 Using prediction tools[38-40], we determined that Mieap has four IDRs occurring around two
203 coiled-coil (CC) domains (amino acids 92–311: IDR1 to IDR3) and in the C-terminus (amino acids
204 499–538: IDR4) (Fig. 2b – e), suggesting that Mieap can potentially drive LLPS[3].
205 All four IDRs are enriched in arginine (R, positively charged) and serine (S, uncharged polar)
206 (Fig. 2b). Additionally, IDR1 is enriched in aspartic acid (D, negatively charged), and IDR2 is
207 enriched in glutamic acid (E, negatively charged). D and E were mixed with positively charged
208 residues in IDR1 and IDR2, respectively. In contrast, IDR3 and IDR4 formed clusters of positively
209 charged residues, characterized by repeats of R and S (Fig. 2b – e) [41].
210 Although amino acid sequences of the IDRs are evolutionarily divergent compared to the
211 structured regions, the distribution of IDRs and clusters of positively charged residues in IDR3 and
212 IDR4 are evolutionarily conserved (Fig. 2c, e, and Supplementary Fig. 2)[41]. In addition, there is an
213 evolutionarily conserved hydropathic character in the Mieap sequence as a whole, the N-terminal half
214 being hydrophilic and the C-terminal half being hydrophobic (Fig. 2d, e, and Supplementary Fig. 2)
215 [42]. This implies that Mieap protein may act as a cellular biosurfactant.
216 These molecular features in Mieap IDRs are consistent with the concept of the "evolutionary
217 signature" that Zarin et al. previously proposed[43]. They found that although the amino acid sequences
218 of IDRs are poorly conserved in alignment, most disordered regions contain multiple molecular
219 features that are preserved as an "evolutionary signature", which can be used to predict IDRs from
220 their amino acid sequences in yeast.
221
222 **Material state and dynamics of Mi-BCs are determined by specific regions of Mieap**
223 To map sites responsible for the physical state and dynamics of Mi-BCs, using a confocal microscope,
224 we examined cells expressing EGFP-Mieap WT (WT) and three deletion-mutant forms, EGFP-Mieap
225 ΔCC, Δ275, and Δ496 (ΔCC, Δ275, and Δ496) (Fig. 3a).
226 All deletion mutants formed condensates, exhibiting distinctive morphologies (Fig. 3b and
227 Supplementary Movie 4). WT formed spherical or oval condensates that assemble near the nucleus
228 and reveal multi-phase structures. In contrast, ΔCC formed lobular condensates near the nucleus,

229 which reveal the single-phase structures. Δ275 formed spherical condensates without the Mieap-
230 depleted phase, which are distributed throughout the cytoplasm. Δ496 formed spherical, multi-phase
231 condensates, which are similar to, but smaller and more numerous than WT condensates.
232 We further examined the relationship between localization of each mutant condensate and
233 mitochondria by performing live-cell imaging of mutants using MitoTracker Red. WT, ΔCC, and
234 Δ496 condensates appeared in mitochondria, whereas Δ275 condensates were detected in the
235 cytoplasm away from mitochondria (Fig. 3c and Supplementary Moive 4).
236 These results suggest that the N-terminal region, containing IDRs (IDR1–3) and spreading over
237 the CC domains, endows Mi-BCs with liquid-like properties. The structured region allows Mi-BCs
238 to reside in mitochondria, and the C-terminal region, containing IDR4, endows Mi-BCs with the
239 capacity to coalesce.
240 To investigate protein dynamics in Mi-BCs, we performed fluorescence recovery after
241 photobleaching (FRAP) studies for WT, ΔCC, Δ275, and Δ496 condensates. During observations up
242 to 60 s after spot-bleaching, with the bleaching depth being 82.2±8.1%, fluorescence intensity of WT,
243 ΔCC, Δ275, and Δ496 condensates recovered to 9.9±4.0%, 4.0±1.0%, 94.3±4.0%, and 17.8±3.1% of
244 their initial values, respectively (Fig. 3d and Supplementary Fig. 3a). Fluorescence recovery of the
245 Δ275 condensates almost achieved their initial value within the 60-s observation period, indicating
246 the most fluid state.
247 When we performed less intense laser exposure, which reduced the bleaching depth to
248 21.2±4.4%, fluorescence recovery increased 60 s after spot-bleaching (WT, 50.4±8.8%; ΔCC,
249 32.6±8.8%; Δ275, 94.9±13.7%; Δ496, 61.5±10.1%) (Supplementary Fig. 3b). The fluorescence
250 recovery rate increased when the number of bleached molecules was small, suggesting that
251 availability may be a rate-limiting factor.
252 We further examined slow fluorescence recovery up to 15 min. WT and Δ496 condensates
253 showed continuous fluorescence recovery, which reached 80.4±10.2% and 94.0±9.5% of the initial
254 value within 15 min, respectively (Fig. 3e). In contrast, ΔCC condensates reached equilibrium at
255 37.4±6.3% of their initial value within 15 min (Fig. 3e). These data suggested that WT condensates,
256 as well as Δ496 condensates, consist mainly of mobile materials, but protein availability from their
257 surroundings is limited. Therefore, FRAP analysis data suggested that Mi-BCs exist in mitochondria.
258
259 **Mieap may phase-separate mitochondrial CL and CL-binding proteins**
260 To identify molecules targeted for phase separation by Mi-BCs, we screened available fluorescence-
261 tagged mitochondrial proteins and mitochondrial fluorescence probes using confocal live-cell
262 imaging. EGFP-BNIP3, EGFP-NIX, AcGFP1-Mito, DsRed2-Mito, and SYBR Green I (a probe for
263 mitochondrial DNA) were localized at mitochondria, but none of them were incorporated into to Mi-
264 BCs (Fig. 4a – e, and Supplementary Fig. 4a, b, and Movie 5).
265 However, 10-N-nonyl acridine orange (NAO) and EGFP-cytochrome *c* were specifically
266 incorporated into Mi-BCs (Fig. 4f, g and Supplementary Fig. 4c and Movie 6). NAO targets CL[44],
267 and cytochrome *c* is a CL-binding protein[21]. As described above, positively charged residues are

enriched in Mieap IDRs (Fig. 2b – e). CL carries a net negative charge[45]. Sequence data reveal the amphiphilicity of Mieap (Fig. 2d – e), and Mi-BCs consist of an electron-dense phase that is positive for OsO_4[46], according to TEM analysis (Supplementary Fig. 1d), suggesting that Mi-BCs may contain unsaturated lipids. This speculation was further supported by Nile-Red staining (Supplementary Fig. 5a, b). Therefore, we suspected that CL is a bona-fide target for phase separation by Mi-BCs.

CL forms complexes with >60 mitochondrial proteins, such as cytochrome *c*, ATP synthase, and the prohibitin complex[47]. Among them, ATP5F1B, which is a subunit of the ATP synthase complex, and PHB2 were previously listed as candidates for "Mieap-binding" proteins in our Mieap-interactome data[48]. This prompted us to investigate whether additional CL-binding/related proteins (ATP5F1B and PHB2) are phase separated by Mi-BCs.

EGFP-ATP5F1B and EGFP-PHB2 localized at mitochondria and then became distributed in Mi-BCs (Fig. 4h, i, and Supplementary Fig. 4d, e, and Movie 6). We confirmed that another subunit of the ATP synthase complex, ATP5F1A, is also incorporated into Mi-BCs, suggesting that the entire ATP synthase may exist in Mi-BCs (Supplementary Fig. 6a, b). Although EGFP-cytochrome *c*, EGFP-ATP5F1A and EGFP-ATP5F1B co-localized with TagRFP-T-Mieap, they were excluded from the Mieap-containing phase and they accumulated in the Mieap-depleted phase in Mi-BCs. These results imply that CL-binding/related proteins are phase separated, but that they are incorporated into Mi-BCs in association with CL.

To determine whether Mieap binds directly to CL, we performed a fat blot assay[49], in which binding of GST-Mieap to CL, phosphatidylcholine (PC), and phosphatidylethanolamine (PE) was evaluated on lipid-dotted membranes. GST-Mieap bound to CL, but not to PC or PE (Fig. 4j).

Mi-BCs compartmentalize and facilitate CL metabolic reactions

We performed mass spectrometric analyses of CL in A549 cells with and without overexpression of Mieap by Ad-Mieap infection. The total amount of CL per cell was higher in Ad-Mieap infected cells than in cells without the infection (Fig. 5a). Broad CL species showed higher absolute values in cells infected with Ad-Mieap than in non-infected cells (Fig. 5b and Supplementary Data 1). In contrast, relative amounts of most CL species did not change. However, Mieap significantly increased the proportions of CL72:5, CL72:6, CL70:6, CL68:5, and CL68:6 (Fig. 5b). These results suggest that Mieap is involved in CL metabolism. Therefore, we speculated that Mi-BCs may function as MLOs to compartmentalize and facilitate CL metabolic reactions. To validate this hypothesis, we examined whether Mi-BCs phase-separate enzymes sequentially involved in CL metabolism (Fig. 5c).

Thus, we examined involvement of the following EGFP-tagged enzymes required for CL metabolism in Mi-BCs by performing confocal live-cell imaging: EGFP-TAMM41, EGFP-PGS1, EGFP-PTPMT1, and EGFP-CRLS1 (involved in CL biosynthesis); EGFP-PLA2G6 (related to CL hydrolysis by phospholipase A_2 activity); and EGFP-TAZ (involved in CL remodeling). All of these enzymes localized at mitochondria and were subsequently incorporated into Mi-BCs (Fig. 5d – i, and Supplementary Fig. 7a – f, and Movie 7). Interestingly, all of these CL metabolic enzymes tended to be concentrated in the Mieap-depleted phase in Mi-BCs (Fig. 5d – i, and Supplementary Movie 7).

We further examined three additional mitochondrial proteins, PRELI (EGFP-PRELI), mitochondrial protease LONP1 (EGFP-LONP1), and mitochondrial CL hydrolase/mitochondrial phospholipase (MitoPLD)/phospholipase D6 (EGFP-PLD6). PRELI is a mitochondrial carrier of PA for CL production[23]. LONP1 is a AAA mitochondrial protease[50]. PLD6 hydrolyzes CL to generate PA at the outer mitochondrial membrane[51]. EGFP-PRELI was incorporated into Mi-BCs (Fig. 5j, and Supplementary Fig. 7g and Movie 7), suggesting that Mi-BCs can also be supplied with PA as a substrate for CL synthesis (Fig. 5C). Both EGFP-LONP1 and EGFP-PLD6 were located at mitochondria, but neither was incorporated into Mi-BCs (Fig. 5k, l, and Supplementary Fig. 7h, i, and Movie 7).

Both N-terminal hydrophilic and C-terminal hydrophobic regions of Mieap are required to generate the multi-phase structure of Mi-BCs

Since CL biosynthetic enzymes and NAO are located at the inner mitochondrial membrane, we assumed that 3D imaging analysis of the relationship between Mi-BCs and enzymes/NAO would provide the most definitive information on the location of Mi-BCs at mitochondria.

Using fluorescence-tagged CL biosynthetic enzymes, we tried to confirm whether the enlarged Mi-BCs are truly localized within mitochondria by performing live-cell imaging analysis with tomographic 3D reconstruction. As shown in Fig. 6a and Supplementary Movies 8 and 10, enlarged Mi-BCs are fully enveloped by EGFP-TAMM41, signals of which are continuously localized from tubular mitochondria to all around the surfaces of spherical Mi-BCs. Supporting the results of CL biosynthetic enzymes, we further confirmed that NAO is also continuously localized from tubular mitochondria, all round and inside of spherical Mi-BCs (Fig. 6b and Supplementary Movies 9 and 10).

Since EGFP-CRLS1 tends to localize at the surface of Mi-BCs, we compared signals of mApple-TOMM20 (the outer mitochondrial membrane) and EGFP-CRLS1 (the inner mitochondrial membrane) around Mi-BCs. As shown in Supplementary Fig. 8a – d, the signals of EGFP-CRLS1 were always detected inside the signals of mApple-TOMM20, compared to those of PLD6 (the outer mitochondrial membrane), suggesting that Mi-BCs are present within mitochondria, possibly facing the inner mitochondrial membrane at their surfaces. Similar results were obtained from the same analysis using another probe for EGFP-TAMM41 (Supplementary Fig. 8e).

Similarly, using EGFP-TAMM41 and NAO as mitochondrial probes, we determined whether ΔCC, Δ275 and Δ496 BCs are located inside mitochondria. As shown in Fig. 6c, e and Supplementary Movies 8 and 10, both ΔCC and Δ496 BCs are also fully enveloped by EGFP-TAMM41, whose signals are continuously derived from tubular mitochondria. Moreover, ΔCC and Δ496 BCs are also stained by NAO as a clear picture of tubular mitochondria and each condensate (Fig. 6f, h and Supplementary Movies 9 and 10). On the other hand, Δ275 condensates are never related to the signals of EGFP-TAMM41 or NAO (Fig. 6d, g and Supplementary Movies 8 – 10). These results suggest that ΔCC and Δ496 BCs are located inside mitochondria, whereas Δ275 BCs are present outside mitochondria.

346 We further examined partitioning behaviors of WT, ΔCC, Δ275, and Δ496 proteins by
347 performing analysis of Intensity Ratios (IRs) of each protein in BCs and cytoplasm[52]. As shown in
348 Fig. 6i, IR values (condensates/cytoplasm) of WT, ΔCC, and Δ496 are 158.62±40.74, 178.81±34.07,
349 8.29±1.92, and 153.14±25.66 (mean±SD), respectively. This implies that IR of WT, ΔCC, and Δ496
350 are more than 18 times higher than that of Δ275. All WT, ΔCC, and Δ496 BCs are localized within
351 mitochondria, whereas Δ275 condensates are present in cytoplasm. Therefore, these IR results
352 suggest that Mieap protein tends to be highly partitioned and concentrated in mitochondrial BCs, and
353 that this propensity is possibly determined by the C-terminal hydrophobic region of Mieap, which
354 could mediate interaction of Mieap with CL/CL-related phospholipids.
355 To explore the mechanism responsible for multi-phase structure in Mi-BCs, using EGFP-
356 TAMM41, we examined whether CL metabolic enzymes are phase-separated by ΔCC, Δ275, and
357 Δ496 condensates (Fig. 7a – d). As expected, Δ275 condensates did not phase-separate EGFP-
358 TAMM41 (Fig. 7c). Importantly, although both ΔCC and Δ496 are located in mitochondria, EGFP-
359 TAMM41 was phase-separated and incorporated in the Mieap-depleted phase of Δ496 condensates
360 (Fig. 7d), whereas EGFP-TAMM41 was mainly localized across the surfaces of ΔCC condensates,
361 which did not generate multi-phase structures (Fig. 7b). These results suggest that both the N-terminal
362 hydrophilic and C-terminal hydrophobic regions are required to form multi-phase droplets. The
363 region of IDR1-3 and two CCs may be critical to the interaction with CL metabolic enzymes to
364 generate the internal enzyme-containing phase (the Mieap-deficient phase) in Mi-BCs.
365 We further explored the internal structure of the Mieap-depleted phase with EFGP-PGS1 or
366 EGFP-TAMM41. Importantly, we found that CL biosynthetic enzymes, EGFP-PGS1 or EGFP-
367 TAMM41, formed condensates in the Mieap-depleted phase, which wetted the interface between the
368 Mieap-containing phase and the Mieap-depleted phase in either WT or Δ496 BCs (Fig. 7e – l). These
369 results suggest that enzymatic reactions between CL metabolic enzymes and their substrates may
370 occur at the interface between the Mieap-containing phase (Mieap and substrates) and the Mieap-
371 depleted phase (CL metabolic enzymes).
372
373 **Mieap functions in mitochondrial quality control via regulation of CL metabolism**
374 CL alterations cause mitochondrial dysfunction[22,25]. Mieap is thought to be involved in mitochondrial
375 quality control[29,30,32,35]. Therefore, we hypothesized that Mieap contributes to mitochondrial quality
376 control by regulating CL metabolism. To test this hypothesis, we evaluated mitochondrial status
377 relative to CL integrity in the presence or absence of Mieap protein in cells and mice.
378 First, we examined respiration rate, mitochondrial ATP production rate, crista morphology, and
379 ROS levels, in control and Mieap-knockdown (KD) LS174T cells under physiological conditions, all
380 of which reflect CL integrity. Flux analysis indicated that respiration and ATP production rates of
381 Mieap-KD cells were significantly lower than those of control cells (Fig. 8a, b). TEM analysis
382 revealed that cristae of Mieap-KD cells decreased, and their morphology became indistinct and
383 irregular, compared to that of control cells (Fig. 8c, d). ROS levels increased in Mieap-KD cells
384 (Supplementary Fig. 9). Consistently, the total amount of CL in control cells was higher than in

Mieap-KD cells (Fig. 8e), and control cells showed higher absolute values for CL species than Mieap-KD cells (Fig. 8f and Supplementary Data 1). Furthermore, physiological Mieap significantly increased the relative values of CL72:4, CL72:5, CL70:4, , CL68:3, and CL68:4 in LS174T cells (Fig. 8f).

Second, utilizing a Mieap-deficient colorectal cancer cell line HCT116[29], we examined whether overexpression of Mieap affects respiration rate and mitochondrial ATP production rate in these cells. As shown in Fig. 8g – j, overexpression of Mieap significantly enhanced respiration rate and mitochondrial ATP production in HCT116 cells.

Third, we analyzed crista morphology in kidney and liver tissues of Mieap-knockout (KO) mice by performing TEM analysis. In Mieap$^{-/-}$ kidney mitochondria, irregularly dilated lamellar structures without distinct OsO_4 staining were observed (Fig. 8k). A decrease in normal crista structure was a common characteristic of Mieap$^{-/-}$ mitochondria in the kidney and liver (Fig. 8k – n).

Fourth, we performed a large-scale cross-sectional observation of 1,225 Mieap$^{+/+}$, Mieap$^{+/-}$, and Mieap$^{-/-}$ mice to identify long-term consequences of Mieap deficiency. Average body weights of Mieap$^{+/-}$ and Mieap$^{-/-}$ mice were higher than those of Mieap$^{+/+}$ mice throughout their lives (Fig. 9a, b). Differences were prominent during middle and old age, from 44 to 104 weeks (Fig. 9c) (mean value ± SE; Mieap$^{+/+}$ 33.065±0.425 g [n=149], Mieap$^{+/-}$ 34.048±0.302 g [n=295], Mieap$^{-/-}$ 35.090±0.392 g [n=175]), but particularly during middle age, from 53 to 62 weeks (Fig. 9d) (mean value ± SE; Mieap$^{+/+}$ 31.048±0.759 g [n=49], Mieap$^{+/-}$ 33.378±0.496 g [n=115], Mieap$^{-/-}$ 34.579±0.645 g [n=68]).

We further evaluated whether there is any difference in obesity between male and female in Mieap-deficient mice. As shown in Supplementary Fig. 10a, b, e, f, Mieap-deficient mice of both sexes developed obesity that persisted throughout their lives. This obesity was prominent during middle and old age, from 44 to 104 weeks (Supplementary Fig. 10c, g) (mean value ± SE; Mieap$^{+/+}$ 36.060±0.509 g [n=74], Mieap$^{+/-}$ 36.835±0.371 g [n=139], Mieap$^{-/-}$ 37.679±0.461 g [n=90] in male, and Mieap$^{+/+}$ 30.110±0.514 g [n=75], Mieap$^{+/-}$ 31.565±0.356 g [n=156], Mieap$^{-/-}$ 32.350±0.483 g [n=85] in female), but more remarkably during middle age, from 53 to 62 weeks (Supplementary Fig. 10d, h), (mean value ± SE; Mieap$^{+/+}$ 34.365±0.952 g [n=23], Mieap$^{+/-}$ 36.714±0.633 g [n=52], Mieap$^{-/-}$ 37.238±0.731 g [n=39] in male, and Mieap$^{+/+}$ 28.113±0.813 g [n=26], Mieap$^{+/-}$ 30.625±0.522 g [n=63], Mieap$^{-/-}$ 31.002±0.770 g [n=29] in female).

To confirm that the body weight gain in Mieap-deficient mice reflects increased fat deposition, we evaluated the amount of subcutaneous fat and intra-abdominal fat (perigonadal fat and perirenal fat) in four representative litter pairs (Mieap$^{+/+}$ and Mieap$^{-/-}$). As shown in Supplementary Fig. 11a – d, the amount of fat in Mieap$^{-/-}$ mice is obviously higher than in Mieap$^{+/+}$ mice in all four pairs. Therefore, we suggest that the body weight gain in Mieap-deficient mice is due to obesity.

Reduced mitochondrial respiratory activity in adipose tissues has been suggested as a factor contributing to obesity[53]. Brown fat tissue (BAT) is essential to heat production via both its respiratory activity, which generates a proton gradient, and uncoupling protein 1 (UCP1)-mediated proton leakage across the mitochondrial inner membrane[54,55]. Therefore, BAT mitigates obesity. Importantly,

as a CL-binding protein, activity of UCP1 is stabilized by CL[56]. Thus, we examined the status of mitochondrial cristae in BAT of Mieap$^{-/-}$ mice. We confirmed that normal crista structure was significantly decreased in Mieap-deficient BAT (Fig. 9e, f), suggesting that obesity may be a long-term consequence of mitochondrial dysfunction due to CL alteration in tissues of Mieap-deficient mice, including BAT.

Finally, we examined endogenous Mieap expression *in vivo*. To achieve this, utilizing WT, Mieap-KO, and p53-KO mice and anti-mouse Mieap antibody, we performed immunohistochemical (IHC) analysis on 20 tissues/organs, including brain (cerebellar cortex), brain (cerebroventricle), heart, liver, kidney, lung, stomach, small intestine, pituitary gland, eye, harderian gland, salivary gland, thyroid, bladder, testis, epididymis, seminal vesicle, prostate, uterus, and fallopian tube. Specific signals of Mieap were detected in all examined tissues/organs by comparing data from WT and Mieap-KO (Supplementary Fig. 12a – t). Interestingly, basal expression of endogenous Mieap protein is not regulated by p53. Importantly, patterns of Mieap expression are remarkably similar to those of cytochrome *c* in IHC and IF (Supplementary Fig. 12a – t), suggesting that endogenous Mieap protein is localized at mitochondria.

We further analyzed expression levels of endogenous Mieap in representative six tissues/organs, including testis, heart, kidney, liver, stomach, and lung, by western blot (WB). Although signals of endogenous Mieap were detected in all six tissues by IHC, we could not find specific bands in liver, kidney, heart, and stomach with WB (Supplementary Fig. 13a, b). Combined with results in IHC and WB, we suggest that physiological Mieap protein is expressed and localized in mitochondria in all tissues/organs, but its expression levels are low in most tissues/organs.

In IHC and WB, we confirmed that endogenous Mieap protein was highly expressed in testis. To validate whether fluorescence-tagged Mieap protein behaves identically to endogenous Mieap, using mNeonGreen-Mieap knock-in (KI) mice, we compared localization of mNeonGreen-tagged Mieap and endogenous Mieap in the testis. As shown in Supplementary Fig. 14a, b, mNeonGreen-tagged Mieap protein was detected at the midpiece of sperm in the testes of KI mice, localization of which was completely consistent with that of endogenous Mieap protein in B6 mice. This result suggests that fluorescence-tagged Mieap protein reflects the behavior of endogenous Mieap protein *in vivo*.

Considering the IR results, although endogenous Mieap protein is expressed at low levels in most tissues/organs, even low expression levels of Mieap protein could be highly concentrated in mitochondrial droplets under physiological conditions. This implies that physiological Mieap protein likely has a significant impact on mitochondrial quality control in all tissues/cells containing mitochondria. On the basis of all these results, we suggest that Mieap maintains mitochondrial quality by regulating CL metabolism.

460 **Discussion**

461 Although the importance of multi-enzyme complexes in metabolic enzyme reactions has been
462 recognized, it remains unclear how this complex of enzymes efficiently and safely enables sequential
463 enzymatic reactions by preventing diffusion of intermediates. A recent report suggested that
464 concentration of multiple enzymes and substrates/intermediates in a restricted space could mediate
465 efficient sequential enzymatic reactions by preventing diffusion of intermediates[57]. In that model,
466 multiple copies of upstream and downstream enzymes involved in sequential enzymatic reactions are
467 assembled into a single cluster, called an "agglomerate." According to this model, "once an upstream
468 enzyme produces an intermediate, although the probability of the intermediate being processed by
469 any individual downstream enzymes is low, the probability that the intermediate will be processed by
470 one of the many downstream enzymes in the 'agglomerate' can be high."[57] Therefore, based on this
471 model, molecular crowding of enzymes, substrates, and intermediates in a restricted space could
472 enable efficient sequential enzymatic reactions mediated by multiple enzymes.

473 The "agglomerate" concept is promising, but an important question remains. How can so many
474 diverse molecules, including multiple enzymes, substrates, and intermediates, be gathered,
475 concentrated, and compartmentalized in a single restricted space? What drives formation of the
476 "agglomerate"? We speculate that BCs could organize agglomerates as metabolic BCs[58].
477 Accumulating evidence suggests that BCs function as MLOs, which promote biochemical reactions
478 by concentrating and compartmentalizing enzymes and substrates in cells[59-63]. Since BCs are not
479 surrounded by lipid bilayers, theoretically, they exhibit spatiotemporal dynamic properties within a
480 cell in response to cellular stress and/or subcellular circumstances. More importantly, while BCs
481 contain hundreds of molecules, a few scaffold proteins can drive formation of these MLOs[1]. If there
482 are proteins that can organize metabolic BCs as scaffolds[61], these agglomerates could enable efficient
483 metabolic reactions.

484 In the present study, we obtained the following evidence supporting our hypothesis that Mi-
485 BCs may regulate CL metabolism: [1] Mieap drives formation of droplets in mitochondria. [2] Mi-
486 BCs may phase-separate CL. [3] Mi-BCs phase-separate all four sequential enzymes for CL
487 biosynthesis (TAMM41, PGS1, PTPMT1, and CRLS1). [4] Mi-BCs phase-separate two enzymes for
488 CL remodeling (PLA2G6 and TAZ). [5] Mi-BCs phase-separate at least three CL-related proteins
489 localized at or near the inner mitochondrial membrane (cytochrome *c*, PHB2, ATP5F1B, and
490 ATP5F1A). [6] The presence or absence of Mieap protein is closely related to an increase or decrease
491 in various species of CL, respectively. [7] Mieap protein specifically increases the proportion of
492 several species of CLs. [8] Mieap deficiency is related to changes in crista structure and CL
493 metabolism in cells, and crista structure *in vivo*. This evidence suggests that Mieap is a scaffold
494 protein that drives formation of metabolic BCs to compartmentalize and concentrate enzymes,
495 substrates, and intermediates that are involved in CL biosynthesis and remodeling, leading to
496 molecular crowding within Mi-BCs that promotes efficient catalysis of CL metabolic reactions.

497 Mi-BCs exhibit properties of multi-phase droplets, in which there are two phases, a Mieap-
498 containing phase and a Mieap-depleted phase. Interestingly, CL and Mieap occur in the Mieap-

containing phase, whereas all CL biosynthesis and remodeling enzymes, including TAMM41, PGS1, PTPMT1, CRLS1, PLA2G6, and TAZ, are predominantly segregated into the Mieap-depleted phase. This result suggests that substrates, intermediates, and products for CL metabolism do not reside in the same phase as their catalytic enzymes. Such a relationship between substrates and enzymes in multi-phase droplets are not limited to Mi-BCs but seen in other droplets. In terms of RNA processing droplets formed by FMRP and CAPRIN1, RNA and phosphorylated FMRP form multi-phase droplets, in which the deadenylation enzyme, CNOT7, and the substrate, polyA-RNA, are segregated into different phases, but this leads to faster deadenylation rates[17].

Why don't substrates and enzymes occur in the same phase of metabolic BCs? A recent study demonstrated that sequestration of enzymes to a membraneless compartment that is away from, but adjacent to substrates, can accelerate reactions much faster than when the enzymes are mixed with the substrates in the same compartment[64]. Concentration of enzymes and substrates in a single phase might result in substrate inhibition[64]. Therefore, separation of enzymes from their substrates via LLPS could facilitate enzymatic reactions by mitigating substrate inhibition. In this case, the interface between the enzyme and substrate phases would be the site of the reaction. Consistent with this hypothesis, we observed accumulation of CL biosynthetic enzymes such as PGS1 and TAMM41 at the interface of the Mieap-depleted phase (Fig. 7e – l). Therefore, enzymatic reactions of CL enzymes and CL substrates may occur at the interface between the Mieap-containing phase (Mieap and substrates) and the Mieap-depleted phase (CL metabolic enzymes) (Fig. 10a – c).

Feric et al. reported the mechanism for generation of multi-phase structures in droplets[65]. By performing *in vivo* and *in vitro* experiments, the authors demonstrated that layered droplet organization is caused by differences in droplet surface tension, facilitating sequential RNA processing reactions in a variety of RNP bodies. In their experiments, F1B and NPM1 formed multi-phase droplets in which F1B droplets tended to be encapsulated within NPM1 droplets. They found that F1B droplets tended to wet hydrophobic surfaces, whereas NPM1 droplets tended to wet hydrophilic surfaces. Wetting refers to the contact between liquids and surfaces, which depends on surface tension. Therefore, in the aqueous phase, F1B droplets with high surface tension tended to be enveloped by NPM1 droplets with lower surface tension.

Since Mieap may be positioned with its N-terminal domain facing outward at the surfaces of Mi-BCs (Supplementary Fig. 1c), Mi-BCs could exist in a hydrophilic environment. If so, according to the theory of Feric et al., the Mieap-containing phase may be enveloped by the Mieap-depleted phase, because the former is more hydrophobic than the latter. However, the authors also pointed out the presence of a surfactant that modulates surface tension alters or inverts the organization of multi-phase droplets. Since Mieap could serve as a biosurfactant, Mieap may modulate the surface tension of the Mieap-containing phase and the Mieap-depleted phase in a hydrophilic environment. Therefore, the relation between the two phases could be inverted in Mi-BCs.

We hypothesize the following model for sequential CL-metabolic reactions promoted by Mieap (Fig. 10a – c). Mieap may stably interact with the substrate (PA) via its C-terminal, hydrophobic, structured region, which exhibits a specific, strong interaction. On the other hand,

538 Mieap weakly and transiently interacts with CL-metabolizing enzymes via its N-terminal hydrophilic
539 region, which exhibits multiple interactions. In this model, once Mieap attracts the substrate with its
540 C-terminal region, Mieap enables sequential CL metabolic reactions by transiently interacting with
541 the enzyme corresponding to the substrate at the interface between the Mieap-containing phase and
542 the Mieap-depleted phase, and then changing enzymes until mature CL is produced. Therefore,
543 interactions of the N-terminal hydrophilic region of Mieap with CL enzymes and the C-terminal
544 hydrophobic region of Mieap with CL/CL-related phospholipids may be critical to drive formation
545 of multi-phase organization of Mi-BCs. In summary, (1) concentration of enzymes and substrates, (2)
546 segregation of enzymes and substrates into distinct sub-compartments of metabolic droplets, (3)
547 interfacial catalysis, and (4) biosurfactant activity of Mieap could foster highly efficient sequential
548 enzymatic reactions for CL metabolism in Mi-BCs. We suggest that Mi-BCs may be the first known
549 metabolic MLOs to regulate CL synthesis and remodeling.

550 BCs are often thought to accelerate enzymatic reaction rate by merely increasing local
551 concentrations of enzymes and substrates (mass action). However, Peeples and Rosen reported that
552 concentrating enzymes and substrates alone results in decreasing enzymatic reaction rates by
553 substrate inhibition due to high concentrations of substrates[18]. They demonstrated that in addition to
554 mass action, a scaffold-induced decrease in K_M is critical to accelerate enzymatic reactions in BCs[18].
555 In their synthetic system where the SUMOylation enzyme cascade is recruited into engineered
556 condensates, they showed that having both enzyme and substrate bound simultaneously to proximal
557 sites in a scaffold oligomer, which leads to decreased $K_{M,}$ is required to enhance the enzymatic
558 reaction. Our Mi-BC model is compatible with their findings; however, further investigation of this
559 hypothesis is required.

560 Significant evidence is now emerging to suggest a critical role of Mieap in mitochondrial
561 quality control in response to cellular stresses. Under hypoxic conditions, Mieap-deficient gastric
562 cancer cells exhibit abnormal mitochondrial structure, enhanced migration, and invasion via
563 increased mitochondrial ROS generation[31]. Mieap expression is defective in oncocytic cell tumors of
564 the thyroid, suggesting a causative role in accumulation of abnormal mitochondria in tumor cells[33].
565 Oncocytic tumors are characterized by accumulation of abnormal mitochondria in tumor cells, but
566 the underlying mechanism remains unclear. Recently, Mieap/Spata18 was reported to participate in
567 DNA-damage-induced mitophagy[66]. Results in these studies are largely consistent with our previous
568 observations[29,35]. However, all observations from these studies, as well as our previous work can be
569 explained by the idea that Mieap influences mitochondrial quality control by regulating CL
570 metabolism. The only unaddressed question is whether lysosomes/lysosomal proteins are involved in
571 the function of Mieap. In response, we have now confirmed that EGFP-cathepsin D is localized at
572 mitochondria and then incorporated into Mi-BCs (unpublished data). Although resolving this
573 question will be challenging, we strongly suggest that the mechanism underlying these observations
574 involves regulation of CL metabolism by Mieap.

575 In the present study, we demonstrated that Mieap-deficient LS174T cells exhibited altered CL
576 metabolism, decreased respiration activity, increased ROS levels, and manifested abnormal crista

structure, all of which are consistent with phenotypes induced by CL alteration. We also found that Mieap-deficient mice exhibit decreased numbers and morphological abnormalities of mitochondrial cristae in kidney and liver tissues. Furthermore, our body weight analysis of Mieap$^{+/+}$, Mieap$^{+/-}$, and Mieap$^{-/-}$ mice clarified increased obesity in Mieap-deficient mice, which is likely attributable to mitochondrial dysfunction in various tissues, including BAT. Therefore, we assume that all these phenotypes in Mieap-deficient cells and mice reflect mitochondrial dysfunctions related to abnormal CL metabolism. So far, autophagy and proteostasis are two major mechanisms in mitochondrial quality control[67]. In addition to these, we suggest that the Mieap-regulated pathway is the third mechanism for mitochondrial quality control, in which Mieap maintains integrity of mitochondria by regulating CL metabolism. It accomplishes this through homeostasis of the inner mitochondrial membrane by regulating CL metabolism, stabilizing oxidative phosphorylation, and suppressing mitochondrial ROS generation (Fig. 10d).

Previously, we reported that although Mieap-deficient mice did not suffer from intestinal dysfunction, Mieap-deficient Apc$^{Min/+}$ mice exhibited remarkable intestinal tumor generation and malignant transformation, compared to Mieap-WT Apc$^{Min/+}$ mice[32]. Furthermore, mitochondria in Mieap-deficient tumors revealed abnormal morphology, including fewer cristae and enlarged, spherical mitochondria. These results support the role of Mieap in mitochondrial quality control through control of CL metabolism in response to oncogenic stress. In addition to Apc$^{Min/+}$ mice, we observed a similar effect in a Mieap-deficient gastric cancer mouse model (unpublished data), using *K19-Wnt1/C2mE* transgenic mice[68]. Therefore, Mieap-regulated mitochondrial quality control could be critical in tumor suppression by promoting CL metabolism, which leads to upregulation of respiratory activity and downregulation of mitochondrial ROS generation. Considering the role of Mieap in p53 function, we suggest that Mieap could act as a spatiotemporal and dynamic regulator/modulator of CL metabolism to suppress tumor initiation and progression. Recently, we found that Mieap-deficient sperm in Mieap-KO mice cause *in vitro* infertility due to mitochondrial ROS elevation and impaired sperm motility (unpublished data). Therefore, in addition to cancer and obesity, it is possible that alterations of Mieap-regulated mitochondrial quality control also promote infertility (Fig. 10d).

A recent study reported that PGS1, PTPMT1, and CRLS1 form a large mitochondrial CL synthesis complex in human cells, with a molecular mass of 700-800 kDa[69]. This large CL synthesis complex includes multiple CL-binding proteins. These observations are very similar to our results that Mi-BCs contain all CL synthesis enzymes and several CL-binding proteins. However, IF experiments on PGS1 or CRLS1 in that study indicated that neither PGS1 nor CRLS1 showed visible Mi-BC-like structures in mitochondria[69]. Our results from live-cell imaging of EGFP-fused CL synthesis enzymes, including PGS1 and CRLS1, also showed that none of the EGFP-tagged CL synthesis enzymes exhibit visible Mi-BC-like structures. Therefore, we suggest that under physiological conditions, the minute size of Mi-BCs or possibly layered, membraneless organelles induced by Mieap may compartmentalize and facilitate CL metabolic reactions *in vivo*, efficiently maintaining enzymatic reactions.

Supporting this hypothesis, although the expression levels of endogenous Mieap protein were low, we confirmed specific expression of Mieap protein *in vivo* in 20 tissues/organs that contain mitochondria (Supplementary Fig. 12a – t). Importantly, patterns of endogenous Mieap expression are very similar to those of cytochrome *c*, suggesting that endogenous Mieap protein is localized at mitochondria. On the other hand, the results of IR indicated that Mieap protein is highly concentrated in mitochondrial droplets (Fig. 6i). These results, taken together, imply that, although the physiological Mieap protein is expressed at low levels *in vivo*, it may be condensed into micro-Mi-BCs that are distributed all through mitochondria to promote CL metabolism. Therefore, we suggest that physiological Mieap protein may have a significant impact on mitochondrial quality control in all tissues/cells containing mitochondria. Further investigation is needed to clarify the full picture of physiological membraneless organelles involved in CL metabolism.

628 **Materials and Methods**

629 **Cell lines**

630 The following cell lines were purchased from the American Type Culture Collection: A549 (tissue,
631 lung cancer; gender, male), U373MG (tissue, glioblastoma; gender, male), LS174T (tissue, colon
632 cancer; gender, female), and 293 (tissue, embryonic kidney). A549 cells were cultured in RPMI 1640
633 (Sigma). U373MG, LS174T, and 293 cells were cultured in DMEM (Sigma). All media were
634 supplemented with 10% fetal bovine serum. Cells were maintained at 37°C in a humidified chamber
635 with 5% CO_2. These cell lines have not been authenticated.

636

637 **Mice**

638 Animal experiment protocols were approved by the Committee for Ethics in Animal Experimentation
639 (approved protocol No. T17-043), and experiments were conducted in accordance with Guidelines
640 for Animal Experiments of the National Cancer Center. C57BL/6J WT mice were obtained from
641 CLEA Japan (Tokyo, Japan). Mieap-knockout (Mieap$^{-/-}$) mice were generated using the Cre/loxP
642 recombination system, as previously reported[32]. Briefly, floxed and trapped alleles were generated
643 using a single construct bearing a gene-trap cassette doubly flanked by LoxP and FRT, located
644 between exons 5 and 8 of the mouse Mieap gene, which is located on chromosome 5. Mieap
645 homozygous (Mieap$^{-/-}$) deficient mice were generated by mating breeding pairs of Mieap
646 heterozygous (Mieap$^{+/-}$) mice. p53-deficient mice were a gift from Dr. S. Aizawa, Center for
647 Developmental Biology, RIKEN[70].

648 For generation of N-terminal or C-terminal mNeonGreen-tagged Mieap KI mice, targeting
649 vectors containing the cassette of the 5'UTR-mNeonGreen-Linker-Exon1-intron1-FRT-NEO-FRT-
650 intron1 or the intron10-exon11-intron11-exon12-intron12-exon13-Linker-mNeonGreen-FRT-NEO-
651 FRT-3'UTR were constructed to express N-terminal or C-terminal mNeonGreen-tagged Mieap
652 protein in mice, respectively. Targeting vectors were introduced into ES cells by electroporation.
653 After geneticin selection, positive ES clones were screened by PCR and Southern blot analysis. The
654 positive clones were injected into C57/B6 mouse blastocysts. The obtained heterozygous and
655 homozygous mice were subjected to analysis.

656 All mice were housed at 22 ± 2°C with a 12 h light/dark cycle with free access to food, CE-
657 2 (CLEA Japan), and water.

658

659 **Establishment of KD cell lines**

660 We established a Mieap-KD cell line using LS174T, as previously described[29]. Mieap expression was
661 inhibited in this cell line by retroviral expression of short-hairpin RNA (shRNA) against the Mieap
662 sequence (Supplementary Fig. 15a, b). We also established LS174T-cont cells using a retroviral
663 vector with a target sequence for EGFP, or an empty retroviral vector, and A549-cont cells using an
664 empty retroviral vector.

665

666 **Plasmid construction**

667 ***Constructs containing Mieap***

668 For construction of the plasmid containing N-terminal EGFP-tagged Mieap, the nucleotide sequence
669 of Mieap was PCR-amplified using primers N-EGFP-Mieap-F and N-EGFP-Mieap-R. PCR products
670 were digested with Kpn I and ligated into pEGFP-C1 (Clontech) cut with the same enzyme. For
671 construction of the plasmid containing C-terminal EGFP-tagged Mieap, the nucleotide sequence of
672 Mieap, excluding the stop codon, was PCR-amplified using the primers C-EGFP-Mieap-F and C-
673 EGFP-Mieap-R. PCR products were ligated into the pCR-Blunt II-TOPO vector (Thermo Fisher
674 Scientific) and sequenced. Inserted products were excised using Hind III restriction sites, and ligated
675 into pEGFP-N1 (Clontech), cut with the same enzyme. N-terminal EGFP-tagged Mieap was used as
676 EGFP-Mieap, except for Fig. 1a – d and Supplementary Movie 3 where the C-terminal EGFP-tagged
677 Mieap was used.

678 Plasmids containing N-FLAG-Mieap (pN-FLAG-Mieap) were constructed as follows. The
679 nucleotide sequence of Mieap was PCR-amplified using the primers, N-FLAG-Mieap-F and N-
680 FLAG-Mieap-R. PCR products were ligated into the pCR-Blunt II-TOPO vector (Thermo Fisher
681 Scientific) and sequenced. Inserted products were excised using the Kpn I restriction sites and ligated
682 into pre-digested pcDNA3.1 (+) (Thermo Fisher Scientific) cut with the same enzyme. The nucleotide
683 sequence of Mieap was excised from the plasmid using the Hind III and Xho I restriction sites, and
684 ligated into pre-digested pCMV-Tag2A (Agilent) cut with the same enzyme.

685 The plasmid containing C-FLAG-Mieap (pC-FLAG-Mieap) was constructed as follows. The
686 nucleotide sequence of Mieap, excluding the stop codon, was PCR-amplified using the primers, C-
687 EGFP-Mieap-F and C-EGFP-Mieap-R, the same primers used for construction of the plasmid
688 containing C-terminal EGFP-tagged Mieap. PCR products were ligated into the pCR-Blunt II-TOPO
689 vector (Thermo Fisher Scientific) and sequenced. Inserted products were excised using the Hind III
690 restriction site and ligated into pre-digested p3xFLAG-CMV-14 (Sigma Aldrich) cut with the same
691 enzyme.

692 Prior to construction of plasmids containing EGFP-Mieap deletion mutants, point mutations in
693 Bgl II, Sac I, EcoR I, and Pst I restriction sites of the multiple cloning site of pEGFP-Mieap were
694 introduced using QuikChange Site-Directed Mutagenesis Kits (Agilent) with primers Mut-F1, Mut-
695 R1, Mut-F2 and Mut-R2, which were confirmed by DNA sequencing.

696 For construction of plasmids containing EGFP-MieapΔCC (pEGFP-MieapΔCC), the
697 nucleotide sequence of pEGFP-Mieap between two Pst I restriction sites was deleted by digestion
698 with Pst I. The remainder was self-ligated, additionally deleting c.810C using the QuikChange Site-
699 Directed Mutagenesis Kit (Agilent) with primers Mut-F3 and Mut-R3 to make the deletion mutation
700 in-frame.

701 For construction of plasmids containing EGFP-MieapΔ275 (pEGFP-MieapΔ275), the
702 nucleotide sequence of pEGFP-Mieap between the Bgl II and Sma I restriction sites was deleted by
703 digestion using Bgl II and Sma I. After blunting with T4 DNA polymerase (Thermo Fisher Scientific),
704 the remainder was self-ligated.

705 For construction of plasmids containing EGFP-MieapΔ496 (pEGFP-MieapΔ496), the
706 nucleotide sequence of pEGFP-Mieap was deleted between the EcoR I and Kpn I restriction sites by
707 digestion using EcoR I and Kpn I. After blunting with T4 DNA polymerase (Thermo Fisher
708 Scientific), the remainder was self-ligated.
709 For construction of plasmids containing TagRFP-T-Mieap (pTagRFP-T-Mieap), the nucleotide
710 sequence of pEGFP-Mieap between the Nhe I and Xho I restriction sites containing EGFP was
711 replaced with nucleotide sequence of pTagRFP-T-EEA1 (Addgene #42635) between the Nhe I and
712 Xho I restriction sites containing TagRFP-T, by digestion using Nhe I and Xho I.
713 For construction of plasmids containing GST-Mieap (pGST-Mieap), the nucleotide sequence
714 of Mieap (amino acids 99-298) was PCR-amplified using the primers, GST-Mieap-F and GST-
715 Mieap-R. PCR products were ligated into the pCR-Blunt II-TOPO vector (Thermo Fisher Scientific)
716 and sequenced. Products were digested with EcoR I and Xho I, and ligated into pGEX5X-2 (Cytiva).
717 For construction of plasmids containing Mieap ΔCC (pMieap ΔCC), pEGFP-Mieap ΔCC was
718 digested at the Kpn I restriction sites to obtain the nucleotide sequence of Mieap ΔCC, and ligated
719 into pcDNA3.1 (+) (Thermo Fisher Scientific) cut with the same enzyme, Kpn I.
720 For construction of plasmids containing Mieap Δ274 (pMieap Δ274), the nucleotide sequence
721 of Mieap Δ274 was PCR-amplified from pEGFP- Mieap Δ275 using the primers, Δ274-F and Δ274-
722 R. PCR products were digested with Kpn I, and ligated into pcDNA3.1 (+) (Thermo Fisher Scientific)
723 cut with the same enzyme, Kpn I.
724 For construction of plasmids containing Mieap Δ496 (pMieap Δ496), pEGFP-Mieap Δ496 was
725 subjected to inverse PCR using the primers, ΔEGFP-F and ΔEGFP-R to delete the nucleotide
726 sequence of EGFP from pEGFP-Mieap Δ496, and the product was self-ligated using KOD-Plus-
727 Mutagenesis Kit (TOYOBO).
728 Prior to construction of plasmids containing TagRFP-T-Mieap deletion mutants, the nucleotide
729 sequence of TagRFP-T was PCR-amplified using the primers, TagRFP-T-F and TagRFP-T-R. PCR
730 products were digested with Hind III and EcoR V, and ligated into pcDNA3.1 (+) (Thermo Fisher
731 Scientific) cut with the same enzymes (pcDNA-N-TagRFP). The nucleotide sequence of Mieap was
732 PCR-amplified using the primers, G35-F and G35-R. PCR products were digested with EcoRV and
733 PspOMI, and ligated into pcDNA-N-TagRFP cut with the same enzymes (pG35).
734 For construction of plasmids containing TagRFP-T-Mieap ΔCC (pTagRFP-T-Mieap ΔCC),
735 pG35 was subjected to inverse PCR using the primers, ΔCC-F and ΔCC-R, and the product was self-
736 ligated using KOD-Plus-Mutagenesis Kit (TOYOBO).
737 For construction of plasmids containing TagRFP-T-Mieap Δ275 (pTagRFP-T-Mieap ΔCC),
738 pTagRFP-T-Mieap was subjected to inverse PCR using the primers, Δ275-F and Δ275-R, and the
739 product was self-ligated using KOD-Plus-Mutagenesis Kit (TOYOBO).
740 For construction of plasmids containing TagRFP-T-Mieap Δ496 (pTagRFP-T-Mieap Δ496),
741 pG35 was subjected to inverse PCR using the primers, Δ496-F and Δ496-R, and the product was self-
742 ligated using KOD-Plus-Mutagenesis Kit (TOYOBO).
743 All primers are listed in Supplementary Data 2.

744
745
746 ***Other constructs***
747 For construction of plasmids containing EGFP-BNIP3 (pEGFP-BNIP3), plasmids containing FLAG-
748 BNIP3 (pCMV-Tag2B-BNIP3) were constructed in advance. For construction of the pCMV-Tag2B-
749 BNIP3, the nucleotide sequence of BNIP3 was PCR-amplified using the primers, BNIP3-F and
750 BNIP3-R. PCR products were ligated into the pCR-Blunt II-TOPO vector (Thermo Fisher Scientific)
751 and sequenced. Inserted products were digested with EcoR I and Xho I, and ligated into the pre-
752 digested pCMV-Tag2B (Agilent) cut with the same enzyme. The nucleotide sequence of pCMV-
753 Tag2B-BNIP3 was digested at the EcoR I and Xho I restriction sites, and subsequently blunted with
754 T4 DNA polymerase (Thermo Fisher Scientific). pEGFP-C1 (Clontech) was digested with Bgl II,
755 blunted with T4 DNA polymerase, self-ligated, digested with EcoR I and Sma I, and ligated with the
756 fragment of pCMV-Tag2B-BNIP3.
757 For construction of plasmids containing EGFP-NIX (pEGFP-NIX), plasmids containing
758 FLAG-NIX (pCMV-Tag2B-NIX) were constructed in advance. For construction of the pCMV-
759 Tag2B-NIX, the nucleotide sequence of NIX was PCR-amplified using the primers, NIX-F and NIX-
760 R. PCR products were ligated into the pCR-Blunt II-TOPO vector (Thermo Fisher Scientific) and
761 sequenced. Inserted products were digested with EcoR I and Xho I, and ligated into pre-digested
762 pCMV-Tag2B (Agilent) cut with the same enzyme. The nucleotide sequence of pCMV-Tag2B-NIX
763 was digested at the EcoR I and Xho I restriction sites, and subsequently blunted with T4 DNA
764 polymerase (Thermo Fisher Scientific). pEGFP-C1 (Clontech) was digested with Bgl II, blunted with
765 T4 DNA polymerase, self-ligated, digested with EcoR I and Sma I, and ligated with the fragment of
766 pCMV-Tag2B-NIX.
767 Plasmids containing EGFP-cytochrome *c* (pEGFP-cytochrome *c*) were constructed as follows.
768 The nucleotide sequence of cytochrome *c* was PCR-amplified using the primers (Cytochrome *c* -F
769 and Cytochrome *c* -R) as reported by Goldstein et al.[71]. PCR products were ligated into the pCR-
770 Blunt II-TOPO vector (Thermo Fisher Scientific) and sequenced. Inserted products were excised
771 using the EcoR I and BamH I restriction sites, and ligated into pEGFP-C1 (Clontech) cut with the
772 same enzymes.
773 For construction of the plasmid backbone containing EGFP (pN-EGFP), the nucleotide
774 sequence of EGFP, excluding the stop codon, was PCR-amplified using the primers, N-EGFP-F and
775 N-EGFP-R. PCR products were digested with Hind III and BamH I, and ligated into pcDNA3.1 (+)
776 (Thermo Fisher Scientific) cut with the same enzymes.
777 For construction of the plasmid backbone containing EGFP (pC-EGFP), the nucleotide
778 sequence of EGFP was PCR-amplified using the primers, C-EGFP-F and C-EGFP-R. PCR products
779 were digested with BamH I and Not I, and ligated into pcDNA3.1 (+) (Thermo Fisher Scientific) cut
780 with the same enzymes.
781 For construction of plasmids containing EGFP-ATP5F1B (pEGFP-ATP5F1B), the nucleotide
782 sequence of ATP5F1B, excluding the stop codon, was PCR-amplified using the primers, ATP5F1B-

783 F1, ATP5F1B-R1, ATP5F1B-F2, and ATP5F1B-R2. PCR products were digested with Hind III and
784 BamH I and ligated into pC-EGFP cut with the same enzymes.
785 For construction of plasmids containing EGFP-PHB2 (pEGFP-PHB2), the nucleotide sequence
786 of PHB2, excluding the stop codon, was PCR-amplified using the primers, PHB2-F and PHB2-R.
787 PCR products were digested with Nhe I and Kpn I and ligated into pC-EGFP cut with the same
788 enzymes.
789 For construction of plasmids containing EGFP-ATP5F1A (pEGFP-ATP5F1A), the nucleotide
790 sequence of ATP5F1A, excluding the stop codon, was PCR-amplified using the primers, ATP5F1A-
791 F and ATP5F1A-R. PCR products were digested with Nhe I and Hind III and ligated into pC-EGFP
792 cut with the same enzymes.
793 For construction of plasmids containing EGFP-TAMM41 (pEGFP-TAMM41), the nucleotide
794 sequence of TAMM41, excluding the stop codon, was PCR-amplified using the primers, TAMM41-
795 F and TAMM41-R. PCR products were digested with Nhe I and BamH I, and ligated into pC-EGFP
796 cut with the same enzymes.
797 For construction of plasmids containing EGFP-PGS1 (pEGFP-PGS1), the nucleotide sequence
798 of PGS1, excluding stop codon, was PCR-amplified using the primers, PGS1-F and PGS1-R. PCR
799 products were digested with Hind III and BamH I and ligated into pC-EGFP cut with the same
800 enzymes.
801 For construction of plasmids containing EGFP-PTPMT1 (pEGFP-PTPMT1), the nucleotide
802 sequence of PTPMT1, excluding the stop codon, was PCR-amplified using the primers, PTPMT1-F
803 and PTPMT1-R. PCR products were digested with Nhe I and Hind III and ligated into pC-EGFP cut
804 with the same enzymes.
805 For construction of plasmids containing EGFP-CRLS1 (pEGFP-CRLS1), the nucleotide
806 sequence of CRLS1 was PCR-amplified using the primers, CRLS1-F and CRLS1-R. PCR products
807 were digested with BamH I and Not I and ligated into pN-EGFP cut with the same enzymes.
808 For construction of plasmids containing EGFP-PLA2G6 (pEGFP-PLA2G6), the nucleotide
809 sequence of PLA2G6, excluding the stop codon, was PCR-amplified using the primers, PLA2G6-F
810 and PLA2G6-R. PCR products were digested with Nhe I and Kpn I and ligated into pC-EGFP cut
811 with the same enzymes.
812 For construction of plasmids containing EGFP-TAZ (pEGFP-TAZ), the nucleotide sequence
813 of TAZ, excluding the stop codon, was PCR-amplified using the primers, TAZ-F and TAZ-R. PCR
814 products were digested with Nhe I and Kpn I and ligated into pC-EGFP cut with the same enzymes.
815 For construction of plasmids containing EGFP-PRELI (pEGFP-PRELI), the nucleotide
816 sequence of PRELI, excluding the stop codon, was PCR-amplified using the primers, PRELI-F and
817 PRELI-R. PCR products were digested with Nhe I and BamH I and ligated into pC-EGFP cut with
818 the same enzymes.
819 For construction of plasmids containing EGFP-LONP1 (pEGFP-LONP1), the nucleotide
820 sequence of LONP1, excluding the stop codon, was PCR-amplified using the primers, LONP1-F and

821 LONP1-R. PCR products were digested with Hind III and BamH I and ligated into pC-EGFP cut with
822 the same enzymes.
823 For construction of plasmids containing EGFP-PLD6 (pEGFP-PLD6), the nucleotide sequence
824 of PLD6, excluding the stop codon, was PCR-amplified using the primers, PLD6-F and PLD6-R.
825 PCR products were digested with Nhe I and Kpn I and ligated into pC-EGFP cut with the same
826 enzymes.
827 All primers are listed in Supplementary Data 2.
828
829 **Transfection**
830 For transfection, cells were seeded (2×10^5 cells/dish) in 35-mm glass bottom dishes. Plasmids (2 μg
831 /dish) were transfected using FuGENE6 transfection reagent (Promega), according to the
832 manufacturer's instructions.
833
834 **Recombinant adenovirus construction**
835 Ad-Mieap was derived from viruses as previously reported[29,35,72]. Replication-deficient recombinant
836 viruses Ad-EGFP-Mieap, Ad-N-FLAG-Mieap, Ad-C-FLAG-Mieap, Ad-EGFP-MieapΔCC (Δ104-
837 270), Ad-EGFP-MieapΔ275, Ad-EGFP-MieapΔ496, Ad-TagRFP-T-Mieap, Ad-mApple-TOMM20
838 derived from mApple-TOMM20-N-10 (Addgene #54955), Ad-EGFP-BNIP3, Ad-EGFP-NIX, Ad-
839 AcGFP1-Mito, Ad-DsRed2-Mito, and Ad-EGFP-cytochrome *c* were generated from the
840 corresponding plasmid vectors and purified as described previously[73]. Briefly, DNA fragments
841 obtained by restriction of each plasmid vector were blunted using T4 DNA polymerase, ligated into
842 the SmiI site of the cosmid, pAxCAwtit (Takara), which contains the CAG promoter and the entire
843 genome of type 5 adenovirus, except the E1 and E3 regions. Recombinant adenoviruses were
844 generated by *in vitro* homologous recombination in the 293 cell line with the cDNA-inserted
845 pAxCAwtit and the adenovirus DNA terminal–protein complex. Viruses were propagated in the 293
846 cell line and purified by two rounds of CsCl density centrifugation. Viral titers were determined with
847 a limiting dilution bioassay using 293 cells.
848
849 **Adenoviral infection**
850 Infection of cell lines was carried out by adding viral solutions to cell monolayers, incubating them
851 at 37°C for 120 min with brief agitation every 20 min. This was followed by addition of culture
852 medium and return of the infected cells to the 37°C incubator.
853
854 **Immunocytochemistry**
855 For immunocytochemistry, cells were grown on 8-well chamber slides ($1\text{-}4\times10^4$ cells/well) at 37°C
856 in conventional culture medium, and fixed in paraformaldehyde (Supplementary Fig. 1b, 2%;
857 Supplementary Fig. 1c, 4%) for 15 min at room temperature. Slides were incubated with Triton X-
858 100 (Supplementary Fig. 1b, 0.1% for 2 min; Supplementary Fig. 1c, 0.5% for 10 min), and washed
859 3x with phosphate-buffered saline (PBS) at room temperature. Cells were blocked with 3% bovine

860 serum albumin (BSA) in PBS (Supplementary Fig. 1b, for 3 h; Supplementary Fig. 1c, for 2 h), and
861 sequentially incubated with rabbit polyclonal anti-Mieap antibody (1:200), mouse monoclonal anti-
862 GFP antibody (1:200), or mouse monoclonal anti-FLAG antibody (1:1000) for 2 h at room
863 temperature. After washing 3x with PBS, slides were incubated with Alexa Fluor 546 goat anti-rabbit
864 IgG antibody (1:200) or Alexa Fluor 546 goat anti-mouse IgG antibody (1:200) at room temperature
865 (Supplementary Fig. 1b, for 2 h; SSupplementary Fig. 1c, for 1 h). Slides were washed 3x with PBS.
866 Then they were mounted with VECTASHIELD H-1000 (Vector Laboratories) and observed using a
867 FLUOVIEW FV3000 confocal laser scanning microscope (Olympus).
868
869 **Histological analysis**
870 Hematoxylin and eosin (HE) staining was performed using Eosin (CS701, Dako) and Hematoxylin
871 (S2020, Dako). Immunohistochemistry (IHC) was performed as described previously[32]. Briefly, for
872 antigen retrieval, paraffin-fixed sections were autoclaved in citric acid buffer (pH 6.0) at 121 °C for
873 10 min. Sections were treated with 0.3% hydrogen peroxide in methanol for 30 min at room
874 temperature to block endogenous peroxidase activity and incubated with 5% bovine serum albumin
875 (BSA) in 50 mM Tris-buffered saline (pH 7.4) containing 0.05% Triton X-100 (T-TBS) for 1 h at
876 room temperature to block non-specific protein binding sites. Sections were then incubated at 4 °C
877 with the primary antibodies, rabbit polyclonal anti-mouse Mieap antibody (1:1000) [32], and mouse
878 monoclonal anti-cytochrome *c* (ab13575, 1 μg/mL) in TBS-T. After overnight incubation, sections
879 were incubated with EnVision + Dual Link System-HRP reagents (Dako) for 1 h according to the
880 manufacturer's instructions at room temperature and treated with 0.02% DAB (DOJINDO) in 0.05
881 M Tris-HCl buffer (pH 7.6). Finally, sections were counterstained with Hematoxylin (Dako). For
882 immunofluorescence (IF), rabbit polyclonal anti-mouse Mieap antibody (1:1000)[32], and mouse
883 monoclonal anti-cytochrome *c* (ab13575, 1 μg/mL) were used for primary antibodies. Alexa Fluor
884 594 goat antirabbit IgG antibody (1:200) and Alexa Fluor 488 goat anti-mouse IgG antibody (1:100)
885 were used for secondary antibodies. Nuclear staining was performed with Hoechst 33342 (10 μg/mL)
886 or TO-PRO-3 (200 nM).
887
888 **Transmission electron microscopy (TEM)**
889 A549-cont and U373MG cells (4×10^4 cells/24-well plate) were infected with Ad-Mieap. On day 1
890 after infection, cells were fixed in phosphate buffered 2.5% glutaraldehyde and subsequently post-
891 fixed in 1% OsO_4 at 4°C for 2 h. Then, specimens were dehydrated in a graded ethanol series and
892 embedded in epoxy resin. Ultrathin sections (75 nm) were cut with an ultramicrotome. Ultrathin
893 sections stained with uranyl acetate and lead staining solution were observed on a transmission
894 electron microscope H-7500 (Hitachi) at 80 kV.
895 LS174T (control and Mieap-KD) cells cultured under normal conditions were also processed
896 for TEM as mentioned above, with the following modifications. 2% glutaraldehyde was used for
897 prefixation. 2% OsO_4 was used instead for post-fixation. 80-90-nm ultrathin sections were cut and
898 observed on a transmission electron microscope H-7600 (Hitachi) at 100 kV.

Kidney and liver specimens were collected from an 18-week-old WT mouse and a 16-week-old Mieap$^{-/-}$ male mouse. BAT specimens were collected from a 40-week-old WT and a 40-week-old Mieap$^{-/-}$ male mouse. Specimens cut into approximately 3 × 3 × 3 mm^3 were also processed for TEM and processed in the same fashion as the aforementioned A549-cont cells. However, a mixture of 2% paraformaldehyde and 2% glutaraldehyde was used for prefixation.

Post-embedding immunoelectron microscopy

A549-cont cells (2×10^5 cells/35-mm glass bottom dish) were infected with Ad-Mieap. On day 1 after infection, cells were fixed with 4% paraformaldehyde and 0.025% glutaraldehyde in 0.1 M PBS (pH 7.4) for 1 h at 4°C. After fixation, cells were washed with 0.1 M PBS (pH 7.4) for 16 h at 4°C, dehydrated in a graded ethanol series, and infiltrated with LR White resin. Polymerization was performed in TAAB embedding capsules (TAAB) inverted on glass-bottom dishes for 3h at 60°C. Ultrathin sections (75 nm) were collected on nickel grids. After blocking with 3% BSA in PBS for 1 h, sections were incubated with anti-Mieap antibody (1:200) diluted in PBS with 0.05% Triton X-100 for 2h at RT. Sections were washed 8x with 0.15% glycine in PBS, and incubated with goat anti-rabbit IgG 10-nm gold antibody (1:50) diluted in PBS with 0.05% Triton X-100 for 2h at RT. Sections were washed 8x in PBS and fixed with 1% glutaraldehyde in PBS for 5 min. Sections were washed 8x in distilled water. Grids were embedded in a mixture containing 2.7% polyvinyl alcohol and 0.3% uranyl acetate. Sections on grids were observed on a transmission electron microscope H-7500 (Hitachi) at 75 kV.

Amino acid sequence analyses of Mieap protein

We analyzed the phylogenetic spread of Mieap orthologs using OrthoDB v10 (https://www.orthodb.org/)[37]. Multiple sequence alignment for Mieap orthologs was performed using Genetyx ver. 10. Prediction of IDRs in the amino acid sequence of Mieap was done using VL3-BA[39] on the PONDR server (http://www.pondr.com/) and collated with meta-prediction of IDRs using DisMeta (http://www-nmr.cabm.rutgers.edu/bioinformatics/disorder/)[38]. Prediction of coiled-coil regions was done using COILS (https://embnet.vital-it.ch/software/COILS_form.html)[40]. Hydrophobicity of Mieap was analyzed according to the Kyte-Doolittle index[42] using ProtScale (https://web.expasy.org/protscale/)[74]. The linear net charge per residue of Mieap was analyzed using CIDER (http://pappulab.wustl.edu/CIDER/)[41].

Analyses of confocal microscopy image data

Throughout the study, confocal microscopy images were taken with a FLUOVIEW FV3000 confocal laser scanning microscope (Olympus). For validation of the spatial relationship between Mi-BCs and mApple-TOMM20, additional images were taken using a SpinSR10 spinning disk confocal super resolution microscope (Olympus). For Z-stack and time-lapse imaging, a montage of differential interference contrast (DIC) and fluorescence images was created using MetaMorph ver. 7.8

937 (Molecular Devices). 3D reconstruction was performed using cellSens Imaging Software (Olympus).
938 Line-scan profiles were acquired using MetaMorph ver. 7.8 (Molecular Devices).
939
940 **FRAP experiments**
941 EGFP-Mieap, EGFP-MieapΔCC, EGFP-MieapΔ275, and EGFP-MieapΔ496 were expressed in
942 A549-cont cells to generate condensates by infection with Ad-EGFP-Mieap, Ad-EGFP-MieapΔCC,
943 Ad-EGFP-MieapΔ275, and Ad-EGFP-MieapΔ496, respectively. FRAP experiments were performed
944 on a FLUOVIEW FV3000 confocal laser scanning microscope (Olympus), using a 60x/1.4 NA oil
945 immersion objective (Olympus). Condensates were subjected to spot-bleaching or full-bleaching
946 (bleaching entire condensates). For spot-bleaching, the bleaching area was unified to a diameter of
947 1.38 μm. Condensates were imaged for 6 s, acquiring 30 images prior to spot-bleaching or 50 s,
948 acquiring 5 images prior to full-bleaching. Photobleaching employed a 488-nm laser at 10% laser
949 power with 11.6 μs/μm exposure time or 1.4% laser power with 1.4 μs/μm exposure time. Time-
950 lapse images were acquired at 0.2-ms intervals for 60 s or 10 s intervals for 15 min. Spot-bleaching
951 data for each construct were acquired from 15 different condensates. Full-bleaching data of each
952 construct were acquired from 10 different condensates.
953
954 **Calculation of intensity ratio (IR)**
955 To evaluate partitioning of EGFP-Mieap and deletion mutant proteins, EGFP-Mieap WT, ΔCC, Δ275,
956 and Δ496 were expressed in A549-cont cells to generate condensates by infection with Ad-EGFP-
957 Mieap WT, ΔCC, Δ275, and Δ496, respectively. EGFP intensity of condensates and cytoplasm was
958 measured. Because EGFP intensity of these condensates was higher than the intensity of 0.4 mg/mL
959 His-EGFP solution for standard curve, we chose intensity ratio (IR) rather than partition coefficient
960 (PC) for the parameter of this partitioning experiments[52]. IR was calculated as ($I_{condensates}$-
961 $I_{background}$)/($I_{cytoplasm}$-$I_{background}$), where $I_{condensates}$, $I_{cytoplasm}$, and $I_{background}$ are the mean intensities of
962 condensates, cytoplasm, and PBS acquired by the identical conditions (laser wavelength, 488 nm;
963 laser transmissivity, 0.01%; detection wavelength, 500–600 nm; voltage, 350 V) on a FLUOVIEW
964 FV3000 confocal laser scanning microscope (Olympus). IR data were obtained from 40 cells for each
965 construct.
966
967 **Expression and purification of GST and GST-Mieap**
968 *Escherichia coli* (BL21) cells transformed with expression vectors were grown in 200 mL of Luria-
969 Bertani medium at 37°C until the OD600 was between 0.55-0.6. Protein expression was induced with
970 100 μM IPTG, and bacteria were subsequently incubated for 3 h at 25°C. After harvesting bacteria
971 by centrifugation at 3000 × *g* for 10 min at 4 °C, pellets were lysed with lysis buffer (1% Triton X-
972 100 buffered in PBS supplemented with 1 mM Phenylmethylsulfonyl fluoride), and sonicated (20 ×
973 30 s bursts with 10 s rest between bursts). Insoluble material was removed by centrifugation at 10,000
974 rpm for 30 min at 4 °C. Supernatant was incubated with glutathione-Sepharose 4B (Cytiva) pre-
975 equilibrated with lysis buffer at 4°C overnight. After the beads were washed twice with lysis buffer,

proteins were eluted with elution buffer (50 mM glutathione diluted in 50 mM Tris–HCl, pH 8.0), and dialyzed at 4°C overnight against PBS.

Lipid-binding analysis

For lipid-binding analysis, protein-lipid interactions on lipid-spotted membranes were evaluated with fat blot assays[49]. Natural CL, PC, and PE derived from bovine heart (Olbracht Serdary Research Laboratories) were diluted with chloroform/methanol/1N HCl (80:80:1). 1 μL of each diluted lipid was spotted onto PVDF membranes (Cytiva) for antigen-antibody reactions using anti-Mieap antibody or nitrocellulose membranes (Cytiva) for antigen-antibody reactions using an anti-GST antibody to align spots with increasing amounts of lipids ranging from 0-667 pmol. Here, approximate molarities of CL, PC, and PE calculated from molecular weights of tetralinoleoyl CL, distearoyl PC, and distearoyl PC were used, respectively. After membranes were blocked with blocking buffer (3% fatty acid-free BSA diluted in 50 mM Tris–HCl, 150 mM NaCl, pH 7.5) for 1 h, membranes were incubated with 2.5 μg/mL of GST-Mieap or GST protein diluted in blocking buffer containing 0.1% Tween 20 overnight. Membranes were incubated with primary antibody (rabbit anti-Mieap antibody or rabbit anti-GST antibody) diluted in blocking buffer containing 0.06% Tween 20 (1:1000) for 3.5 h, and subsequently a secondary antibody (goat anti-rabbit antibody conjugated to horseradish-peroxidase) diluted in blocking buffer containing 0.06% Tween 20 (1:10000) for 1 h. ECL Western Blotting Detection Reagents (Cytiva) was used to detect HRP and chemiluminescence was visualized with an ImageQuant LAS 4000 system (Cytiva).

Lipid preparation

Lipid preparation was performed as described previously[75,76]. Briefly, total lipids were extracted from samples using the Bligh-Dyer method[77]. An aliquot of the organic phase was added to an equal volume of methanol before being loaded onto a DEAE-cellulose column (Wako Chemical) pre-equilibrated with chloroform. After successive washes with chloroform/methanol (1:1, v/v), acidic phospholipids were eluted with chloroform/methanol/HCl/water (12:12:1:1, v/v), followed by evaporation to dryness to yield a residue was soluble in methanol.

Mass spectrometric analyses of CL

Analyses were performed on an LC/MS/MS system consisting of a Q-Exactive Plus mass spectrometer (Thermo Fisher Scientific) equipped with an electrospray ionization source and an UltiMate 3000 system (Thermo Fisher Scientific). Lipid samples were separated on a Waters X-Bridge C_{18} column (3.5 μm, 150 mm × 1.0 mm i.d.) at 40°C using a solvent step-gradient as follows: mobile phase A (isopropanol/methanol/water (5:1:4, v/v/v) supplemented with 5 mM ammonium formate and 0.05% ammonium hydroxide (28% in water))/mobile phase B (isopropanol supplemented with 5 mM ammonium formate and 0.05% ammonium hydroxide (28% in water)) ratios of 60%/40% (0 min), 40%/60% (1 min), 20%/80% (9 min), 5%/95% (11-30 min), 95%/5% (31-35 min) and 60%/40% (45 min). Flow rate was 25 μL/min. Source and ion transfer parameters

1015 applied were as follows. Spray voltage was 3.0 kV. For negative ionization modes, the sheath gas and
1016 capillary temperatures were maintained at 60 and 320 °C, respectively. The Orbitrap mass analyzer
1017 was operated at a resolving power of 70,000 in full-scan mode (scan range: 200–1800 m/z; automatic
1018 gain control (AGC) target:3e6) and of 35,000 in the Top 20 data-dependent MS2 mode (stepped
1019 normalized collision energy: 20, 30 and 40; isolation window: 4.0 m/z; AGC target: 1e5).
1020 Identification of CL molecular species was performed using LipidSearch 4.2 software (Mitsui
1021 Knowledge Industry).
1022
1023 **Real-time ATP rate assay**
1024 LS174T-cont and Mieap-KD cells were seeded at a density of 2.5×10^4 cells/well (n=9) on a Seahorse
1025 XF24 Cell Culture Microplate. Cells were incubated at 37°C in a humidified chamber with 5% CO_2.
1026 18 h after seeding, culture medium was replaced with XF DMEM medium pH 7.4 supplemented with
1027 25 mM glucose and 2 mM L-glutamine through three washes.
1028 HCT116 cells were seeded at a density of 0.8×10^6 cells/60-mm dish (n=9). Cells were
1029 incubated at 37°C in a humidified chamber with 5% CO_2. 24 h after seeding, cells were treated with
1030 Ad-Mieap or Ad-empty. 24 h after infection, cells were reseeded at a density of 4×10^4 cells/well (n=9)
1031 on a SeahorseXF24 Cell Culture Microplate. 20 h after reseeding, culture medium was replaced with
1032 XF DMEM medium pH 7.4 supplemented with 25 mM glucose and 2 mM L-glutamine through three
1033 washes.
1034 After cells were incubated at 37 °C in a non-CO_2 incubator for 60 min, cell culture plates
1035 were loaded into a Seahorse XFe24 Analyzer. Oxygen consumption rate (OCR) and extracellular
1036 acidification rate (ECAR) were recorded before and after serial injections of oligomycin and
1037 rotenone/antimycin A to yield final concentrations of 0.5 μM.
1038
1039 **Flow cytometric analysis**
1040 LS174T-cont and Mieap-KD cells cultured under normal conditions were harvested by trypsin-EDTA
1041 treatment. After adding complete growth media to inactivate trypsin, cells were centrifuged, washed
1042 with PBS, and incubated with 5 μM 2′,7′-dichlorofluorescin-diacetate (Sigma) for 20 min at 37°C.
1043 After being washed with PBS, cells were immediately analyzed with an EC800 flow cytometry
1044 analyzer (Sony) using the 488-nm line.
1045
1046 **Quantification and statistical analysis**
1047 ***FRAP data quantification***
1048 Fluorescence recovery rates were calculated using cellSens Imaging Software (Olympus), in which
1049 the intensity initially acquired after bleaching was set to 0 and the pre-bleaching intensity was set to
1050 1. The normalized average fluorescence recovery was plotted in JMP 14.2.0 (SAS).
1051
1052 ***Crista data quantification***

For quantification of crista data, crista area and outlines of mitochondrial sections in TEM images were marked manually using Adobe Photoshop CC, where normal crista morphology was identified by the presence of lamellar structures with distinct OsO_4 staining. Aberrant crista-like structures that were not observed in mitochondria of WT were excluded. Subsequently, the ratio of crista area per mitochondrial section was calculated from the indicated number of mitochondria in legends of Fig. 8d, l, m, and 9f, using Image J[78].

Statistical analysis

Statistical analyses were performed in JMP 14.2.0 (SAS). Levels of significance in Figure 6i, 8a, 8b, 8d, 8h–j, 8l, 8n, 9b–d, 9f, S10b–d, S10f–h were assessed using Student's two-tailed t-tests. Levels of significance in mass spectrometric analyses for biological replicate pairs shown in Figure 5a, 5b, 8e, and 8f were assessed using the paired two-tailed t-test. $p < 0.05$ was considered statistically significant. Asterisks were allotted to all the Figures containing statistical analyses as follows: *, $p < 0.05$; **, $p < 0.01$, ***, $p < 0.001$, ****, $p < 0.0001$.

Data visualization

Visualization of the experimental data subjected to statistical analyses were performed using Graph Builder engine in JMP 14.2.0 (SAS). When the data were visualized using violin plots, box plots were overlaid. The center line in the box indicates the median. The bottom and top of the box indicate the 25th and 75th percentiles. The whiskers extend 1.5 times the interquartile range (IQR) from the top and bottom of the box unless the minimum and maximum values are within the IQR. The values which fall above or below the whiskers are plotted individually as outliers.

Data availability

The datasets generated during the mass spectrometric analyses of cardiolipin are included in Supplementary Data 1, and available in the Metabolomics Workbench repository, [https://www.metabolomicsworkbench.org/data/DRCCMetadata.php?Mode=Project&ProjectID=PR001192], under Project ID PR001192. All other relevant data which support the findings of this study are included in this article and its supplementary information files. Source data are provided with this paper.

Code availability

The codes used for data analysis are available from the corresponding author upon a request.

References

1. Shin, Y., and Brangwynne, C.P. Liquid phase condensation in cell physiology and disease. *Science* **357**, eaaf4382 (2017).

2. Boeynaems, S. et al. Protein Phase Separation: A New Phase in Cell Biology. *Trends Cell Biol.* **28**, 420–435 (2018).

3. Alberti, S., Gladfelter, A., and Mittag, T. Considerations and Challenges in Studying Liquid-Liquid Phase Separation and Biomolecular Condensates. *Cell* **176**, 419–434 (2019).

4. Sabari, B.R. et al. Coactivator condensation at super-enhancers links phase separation and gene control. *Science* **361**, eaar3958 (2018).

5. Case, L.B., Zhang, X., Ditlev, J.A., and Rosen, M.K. Stoichiometry controls activity of phase-separated clusters of actin signaling proteins. *Science* **363**, 1093–1097 (2019).

6. Huang, W.Y.C. et al. A molecular assembly phase transition and kinetic proofreading modulate Ras activation by SOS. *Science* **363**, 1098–1103 (2019).

7. Du, M.J., and Chen, Z.J.J. DNA-induced liquid phase condensation of cGAS activates innate immune signaling. *Science* **361**, 704–709 (2018).

8. Woodruff, J.B. et al. The centrosome is a selective condensate that nucleates microtubules by concentrating tubulin. *Cell* **169**, 1066–1077 (2017).

9. Rai, A.K., Chen, J.X., Selbach, M., and Pelkmans, L. Kinase-controlled phase transition of membraneless organelles in mitosis. *Nature* **559**, 211–216 (2018).

10. Welch, G.R. On the role of organized multienzyme systems in cellular metabolism: a general synthesis. *In Prog. Biophys. Mol. Biol.* (London, UK: Elsevier), pp. 103–191 (1977).

11. Srere, P.A. Complexes of sequenctial metabolic enzymes. *Annu. Rev. Biochem*. **56**, 89–124 (1987).

12. Jin, M.Y. et al. Glycolytic Enzymes Coalesce in G Bodies under Hypoxic Stress. *Cell Rep.* **20**, 895–908 (2017).

13. Lee, H., DeLoache, W.C., and Dueber, J.E. Spatial organization of enzymes for metabolic engineering. *Metab. Eng.* **14**, 242–251 (2012).

14. Kohnhorst, C.L. et al. Identification of a multienzyme complex for glucose metabolism in living cells. *J.*

Biol. Chem. **292**, 9191–9203 (2017).

15. Schmitt, D.L., and An, S. Spatial Organization of Metabolic Enzyme Complexes in Cells. *Biochemistry* **56**, 3184–3196 (2017).

16. An, S.G., Kumar, R., Sheets, E.D., and Benkovic, S.J. Reversible compartmentalization of de novo purine biosynthetic complexes in living cells. *Science* **320**, 103–106 (2008).

17. Kim, T.H. et al. Phospho-dependent phase separation of FMRP and CAPRIN1 recapitulates regulation of translation and deadenylation. *Science* **365**, 825-829 (2019).

18. Peeples, W. and Rosen, M.K. Mechanistic dissection of increased enzymatic rate in a phase-separated compartment. *Nat. Chem. Biol.* **17**, 693–702 (2021).

19. Macfarlane, M.G. Structure of cardiolipin. *Nature* **182**, 946 (1958).

20. Ikon, N., and Ryan, R.O. Cardiolipin and mitochondrial cristae organization. *Biochim. Biophys. Acta (BBA)-Biomembranes* **1859**, 1156–1163 (2017).

21. Paradies, G., Paradies, V., De Benedictis, V., Ruggiero, F.M., and Petrosillo, G. Functional role of cardiolipin in mitochondrial bioenergetics. *Biochim. Biophys. Acta (BBA)-Bioenergetics* **1837**, 408–417 (2014).

22. Ren, M.D., Phoon, C.K.L., and Schlame, M. Metabolism and function of mitochondrial cardiolipin. *Prog. Lipid Res.* **55**, 1–16 (2014).

23. Potting, C. et al. TRIAP1/PRELI complexes prevent apoptosis by mediating intramitochondrial transport of phosphatidic acid. *Cell Metab.* **18**, 287–295 (2013).

24. Ye, C., Shen, Z., and Greenberg, M.L. Cardiolipin remodeling: a regulatory hub for modulating cardiolipin metabolism and function. *J. Bioenerg. Biomembr.* **48**, 113–123 (2016).

25. Paradies, G., Paradies, V., Ruggiero, F.M., and Petrosillo, G. Role of cardiolipin in mitochondrial function and dynamics in health and disease: Molecular and pharmacological aspects. *Cells* **8**, 728 (2019).

26. Saric, A., Andreau, K., Armand, A.S., Moller, I.M., and Petit, P.X. Barth syndrome: from mitochondrial dysfunctions associated with aberrant production of reactive oxygen species to pluripotent stem cell studies. *Front Genet.* **6**, 359 (2016).

27. Acehan, D., Xu, Y., Stokes, D.L. and Schlame, M. Comparison of lymphoblast mitochondria from normal

1168 subjects and patients with Barth syndrome using electron microscopic tomography. *Lab Invest.* **87**, 40-48
1169 (2006).
1170
1171 28. Dudek, J. et al. Cardiolipin deficiency affects respiratory chain function and organization in an induced
1172 pluripotent stem cell model of Barth syndrome. *Stem Cell Res.* **11**, 806-819 (2013).
1173
1174 29. Miyamoto, Y. et al. Possible Existence of Lysosome-Like Organella within Mitochondria and Its Role in
1175 Mitochondrial Quality Control. *PLoS One* **6**, e16054 (2011).
1176
1177 30. Kamino, H. et al. Mieap-regulated mitochondrial quality control is frequently inactivated in human
1178 colorectal cancer. *Oncogenesis* **5**, e181 (2016).
1179
1180 31. Okuyama, K. et al. Mieap-induced accumulation of lysosomes within mitochondria (MALM) regulates
1181 gastric cancer cell invasion under hypoxia by suppressing reactive oxygen species accumulation. *Sci. Rep*. **9**,
1182 2822 (2019).
1183
1184 32. Tsuneki, M., Nakamura, Y., Kinjo, T., Nakanishi, R., and Arakawa, H. Mieap suppresses murine intestinal
1185 tumor via its mitochondrial quality control. *Sci. Rep.* **5**, 12472 (2015).
1186
1187 33. Mussazhanova, Z. et al. Causative role for defective expression of mitochondria-eating protein in
1188 accumulation of mitochondria in thyroid oncocytic cell tumors. *Cancer Sci.* **111**, 2814–2823 (2020).
1189
1190 34. Gaowa, S. et al. Possible role of p53/Mieap-regulated mitochondrial quality control as a tumor suppressor
1191 in human breast cancer. *Cancer Sci.* **109**, 3910–3920 (2018).
1192
1193 35. Kitamura, N. et al. Mieap, a p53-Inducible Protein, Controls Mitochondrial Quality by Repairing or
1194 Eliminating Unhealthy Mitochondria. *PLoS One* **6**, e16060 (2011).
1195
1196 36. Feric, M. et al. Self-assembly of multi-component mitochondrial nucleoids via phase separation. *EMBO J.*
1197 **40**, e107165 (2021).
1198
1199 37. Kriventseva, E.V. et al. OrthoDB v10: sampling the diversity of animal, plant, fungal, protist, bacterial and
1200 viral genomes for evolutionary and functional annotations of orthologs. *Nucleic Acids Res*. **47**, D807–D811
1201 (2019).
1202
1203 38. Huang, Y.J., Acton, T.B., and Montelione, G.T. DisMeta: a meta server for construct design and
1204 optimization. *Methods Mol. Biol.* **1091**, 3–16 (2014).
1205
1206 39. Uversky, V.N., Radivojac, P., Iakoucheva, L.M., Obradovic, Z., and Dunker, A.K. Prediction of intrinsic
1207 disorder and its use in functional proteomics. *Methods Mol. Biol.* **408**, 69–92 (2007).

40. Lupas, A., Van Dyke, M., and Stock, J. Predicting coiled coils from protein sequences. *Science* **252**, 1162–1164 (1991).

41. Holehouse, A.S., Das, R.K., Ahad, J.N., Richardson, M.O., and Pappu, R.V. CIDER: Resources to Analyze Sequence-Ensemble Relationships of Intrinsically Disordered Proteins. *Biophys. J.* **112**, 16–21 (2017).

42. Kyte, J., and Doolittle, R.F. A simple method for displaying the hydropathic character of a protein. *J. Mol. Biol.* **157**, 105–132 (1982).

43. Zarin, T. et al. Proteome-wide signatures of function in highly diverged intrinsically disordered regions. *Elife.* **8**, e46883 (2019).

44. Kaewsuya, P., Danielson, N.D., and Ekhterae, D. Fluorescent determination of cardiolipin using 10-N-nonyl acridine orange. *Anal. Bioanal. Chem.* **387**, 2775–2782 (2007).

45. Sathappa, M. and Alder, N.N. The ionization properties of cardiolipin and its variants in model bilayers. *Biochim. Biophys. Acta.* **1858**, 1362-1372 (2016).

46. Belazi, D., Sole-Domenech, S., Johansson, B., Schalling, M., and Sjovall, P. Chemical analysis of osmium tetroxide staining in adipose tissue using imaging ToF-SIMS. *Histochem. Cell Biol.* **132**, 105–115 (2009).

47. Planas-Iglesias, J. et al. Cardiolipin Interactions with Proteins. *Biophys. J.* **109**, 1282–1294 (2015).

48. Miyamoto, T. et al. Identification of 14-3-3γ as a Mieap-interacting protein and its role in mitochondrial quality control. *Sci. Rep.* **2**, 379 (2012).

49. Munnik, T., and Wierzchowiecka, M. Lipid-binding analysis using a fat blot assay. *Methods Mol. Biol.* **1009**, 253–259 (2013).

50. Bota, D.A., and Davies, K.J. Lon protease preferentially degrades oxidized mitochondrial aconitase by an ATP-stimulated mechanism. *Nat. Cell Biol.* **4**, 674–680 (2002).

51. Choi, S.Y. et al. A common lipid links Mfn-mediated mitochondrial fusion and SNARE-regulated exocytosis. *Nat. Cell Biol.* **8**, 1255–1262 (2006).

52. Banani, S.F. et al. Compositional Control of Phase-Separated Cellular Bodies. *Cell.* **166**, 651–663 (2016).

53. Lee, J.H. et al. The role of adipose tissue mitochondria: Regulation of mitochondrial function for the treatment of metabolic diseases. *Int. J. Mol. Sci.* **20**, 4924 (2019).

54. Sidossis, L. and Kajimura S. Brown and beige fat in humans: thermogenic adipocytes that control energy and glucose homeostasis. *J Clin Invest.* **125**, 478–486 (2015).

55. Fenzl, A. and Kiefer, F.W. Brown adipose tissue and thermogenesis. *Horm Mol Biol Clin Investig.* **19**, 25–37 (2014).

56. Crichton, P.G., Lee, Y., and Kunji, E.R. The molecular features of uncoupling protein 1 support a conventional mitochondrial carrier-like mechanism. *Biochimie.* **134**, 35–50 (2017).

57. Castellana, M. et al. Enzyme clustering accelerates processing of intermediates through metabolic channeling. *Nat. Biotechnol.* **32**, 1011–1018 (2014).

58. Prouteau, M., and Loewith, R. Regulation of Cellular Metabolism through Phase Separation of Enzymes. *Biomolecules* **8**, 160 (2018).

59. Strulson, C.A., Molden, R.C., Keating, C.D., and Bevilacqua, P.C. RNA catalysis through compartmentalization. *Nat. Chem.* **4**, 941–946 (2012).

60. Bracha, D., Walls, M.T., and Brangwynne, C.P. Probing and engineering liquid-phase organelles. *Nat. Biotechnol.* **37**, 1435–1445 (2019).

61. Zhao, E.M. et al. Light-based control of metabolic flux through assembly of synthetic organelles. *Nat. Chem. Biol.* **15**, 589–597 (2019).

62. Hinzpeter, F., Gerland, U., and Tostevin, F. Optimal Compartmentalization Strategies for Metabolic Microcompartments. *Biophys. J.* **112**, 767–779 (2017).

63. Su, X. et al. Phase separation of signaling molecules promotes T cell receptor signaltransduction. *Science.* **352**, 595–599 (2016).

64. Kojima, T., and Takayama, S. Membraneless Compartmentalization Facilitates Enzymatic Cascade Reactions and Reduces Substrate Inhibition. *ACS Appl. Mater. Interfaces* **10**, 32782–32791 (2018).

65. Feric, M. et al. Coexisting liquid phases underlie nucleolar subcompartments. *Cell.* **165**, 1686–1697 (2016).

66. Dan, X. et al. DNA damage invokes mitophagy through a pathway involving Spata18. *Nucleic Acids Res.* **48**, 6611–6623 (2020).

67. Tatsuta, T. and Langer, T. Quality control of mitochondria: protection against neurodegeneration and aging. *EMBO J.* **27**, 306-314 (2008).

68. Oshima, H. et al. Carcinogenesis in mouse stomach by simultaneous activation of the Wnt signaling and prostaglandin E-2 pathway. *Gastroenterology* **131**, 1086–1095 (2006).

69. Serricchio, M., Vissa, A., Kim, P.K., Yip, C.M., and McQuibban, G.A. Cardiolipin synthesizing enzymes form a complex that interacts with cardiolipin-dependent membrane organizing proteins. *Biochim. Biophys. Acta-Mol. Cell Biol. Lipids* **1863**, 447–457 (2018).

70. Tsukada, T. et al. Enhanced proliferative potential in culture of cells from p53-deficient mice. *Oncogene.* **8**, 3313–3322 (1993).

71. Goldstein, J.C., Waterhouse, N.J., Juin, P., Evan, G.I., and Green, D.R. The coordinate release of cytochrome c during apoptosis is rapid, complete and kinetically invariant. *Nat. Cell Biol.* **2**, 156–162 (2000).

72. Nakamura, Y. et al. BNIP3 and NIX mediate Mieap-induced accumulation of lysosomal proteins within mitochondria. *PLoS One* **7**, e30767 (2012).

73. Oda, K. *et al.* p53AIP1, a potential mediator of p53-dependent apoptosis, and its regulation by Ser-46-phosphorylated p53. *Cell* **102**, 849–862 (2000).

74. Wilkins, M.R. et al. Protein identification and analysis tools in the ExPASy server. *Methods Mol. Biol.* **112**, 531–552 (1999).

75. Shindou, H. et al. Docosahexaenoic acid preserves visual function by maintaining correct disc morphology in retinal photoreceptor cells. *J. Biol. Chem.* **292**, 12054–12064 (2017).

76. Yamamoto, T. et al. Decrease in membrane phospholipids unsaturation correlates with myocardial diastolic dysfunction. *PLoS One* **13**, e0208396 (2018).

77. Bligh, E.G., and Dyer, W.J. A rapid method of total lipid extraction and purification. *Can. J. Biochem.* **37**, 911–917 (1959).

78. Schneider, C.A., Rasband, W.S., and Eliceiri, K.W. NIH Image to ImageJ: 25 years of image analysis. *Nat. Methods* **9**, 671–675 (2012).

Acknowledgments

We thank H. Suzuki and M. Tsuneki for their contributions to *in vitro* and IHC experiments, respectively. This work was supported by grants from The National Cancer Center Research and Development Fund (29-E-1, 30-A-3), JSPS KAKENHI Grant Numbers JP-19K07655, JP-19K07703, JP-17H06267 and JP-20K20305, and The Naito Foundation.

Author contributions

NI, YN, and HA performed *in vitro* experiments. KH, YS, and YN contributed to animal experiments. NI and HA analyzed data. NI and HA designed the research. NI and HA wrote paper. HA coordinated and supervised the project.

Declaration of interests

The authors declare no competing interests.

1345 **Figure legends**

1346 **Figure 1. Mieap forms liquid droplets in mitochondria.**

1347 (**a**) Confocal microscopy showing the spatial relationship between Mi-BCs (EGFP-Mieap) and
1348 mitochondrial outer membranes visualized with mApple-TOMM20. Left: a cell image. Middle:
1349 higher magnification of the area indicated by the dashed square in the left panel and a line-scan of
1350 fluorescence intensities along the dashed arrow. Right: 3D reconstruction of the cell shown in the left
1351 panel. See also Supplementary Movie 3.

1352 (**b**) Z-stack images of the cell in (**a**).

1353 (**c**) Super-resolution images showing the spatial relationship between Mi-BCs (EGFP-Mieap) and
1354 mitochondrial outer membranes, visualized with mApple-TOMM20.

1355 (**d**) Confocal microscopy showing the spatial relationship between enlarged Mi-BCs and mApple-
1356 TOMM20. Lower right: line-scan as in (**a**). See also Supplementary Movie 3.

1357

1358 **Figure 2. Mieap is an IDR-containing protein**

1359 (**a**) Phylogenetic spread of Mieap orthologs annotated with OrthoDB v10. Red sectors indicate
1360 present species. Light blue sectors indicate missing species.

1361 (**b**) Proportion of amino acid residues in each domain of the Mieap protein.

1362 (**c**) Multiple sequence alignment for Mieap orthologs in representative eukaryotes. Black and gray
1363 boxes indicate 100% and 80% identical residues among eukaryotes, respectively. Blue letters indicate
1364 IDRs annotated by VL3-BA. Orange letters indicate coiled-coil regions annotated by COILS.

1365 (**d**) Schematic of the domain structure of Mieap. The dashed vertical line indicates the boundary of
1366 gross hydrophilic and hydrophobic halves, separated by IDR3 and the adjacent structured region.
1367 Asterisks indicate clusters of positively charged residues.

1368 (**e**) Sequence analyses of Mieap protein. VL3-BA prediction of IDRs on the amino acid sequence of
1369 Mieap, in which bold lines indicate IDRs; DisMeta, meta-prediction of IDRs on the amino acid
1370 sequence of Mieap; COILS; coiled-coil regions annotated on the amino acid sequence of Mieap using
1371 a 21-residue sliding window; Hydro, hydrophobicity of Mieap using a 9-residue sliding window;
1372 NCPR, the linear net charge per residue of Mieap using a 5-residue sliding window.

1373

1374 **Figure 3. Material state and dynamics of Mi-BCs are determined by specific regions of Mieap.**

1375 (**a**) EGFP-Mieap and the three deletion-mutant forms. The schematic indicates wild-type (WT) and
1376 three deletion mutants (ΔCC, Δ275, and Δ496) of EGFP-Mieap protein. Numbers indicate amino acid
1377 residues.

1378 (**b**) Representative images with a cross-sectional slice view of BCs formed by WT, ΔCC, Δ275, and
1379 Δ496 in A549 cells obtained with fluorescent confocal microscopy. See also Supplementary Movie
1380 4.

1381 (**c**) Subcellular localization of BCs formed by WT, ΔCC, Δ275, and Δ496, compared with a
1382 mitochondrial probe MitoTracker Red. See also Supplementary Movie 4.

(**d**) Normalized average fluorescence recovery in the FRAP experiment. Condensates formed by WT, ΔCC, Δ275, and Δ496 were analyzed in A549 cells. Each condensate was subjected to spot-bleaching using a 488-nm laser at 10% laser power with 11.6 μs/μm exposure time and followed up for 60 s. n = 15 condensates for each construct. Data shown are means ±SD.

(**e**) Normalized average fluorescence recovery in the FRAP experiment with weaker laser exposure as in (**d**). Laser power was weakened to 1.4% and exposure time was shortened to 1.4 μs/μm. Observation duration was expanded to 15 min after photobleaching entire condensates. n = 10 condensates for each construct. Data shown are means ±SD.

Figure 4. Mi-BCs phase-separate mitochondrial CL and CL-binding proteins.

(**a** – **i**) Live-cell imaging of Mi-BCs and various mitochondrial fluorescence probes in A549 cells. Whether each mitochondrial fluorescence probe is phase-separated by Mi-BCs was examined with live-cell imaging analysis in A549 cells. EGFP-BNIP3 (**a**), EGFP-NIX (**b**), AcGFP-mito (**c**), DsRed2-mito (**d**), and SYBR Green I (**e**), were not incorporated into Mi-BCs. However, 10-nonylacridine orange bromide (NAO) (**f**), EGFP-cytochrome *c* (**g**), EGFP-ATP5F1B (**h**), and EGFP-PHB2 (**i**) were incorporated into Mi-BCs. Lower right: line-scan of fluorescence intensities along the dashed arrow. See also Supplementary Movies 5 and 6.

(**j**) Lipid-binding analysis of GST-tagged Mieap protein. GST-Mieap or GST was incubated with membranes on which increasing amounts of CL, phosphatidylcholine (PC), and phosphatidylethanolamine (PE), ranging from 0-667 pmol, were spotted. Protein-lipid interactions were visualized using an anti-Mieap antibody and/or anti-GST antibody, as indicated.

Figure 5. Mi-BCs compartmentalize and facilitate CL metabolic reactions.

(**a**) Quantitative assessment of total CL by mass spectrometric analysis. Uninfected A549 cells or cells infected with Ad-Mieap were subjected to mass spectrometric analysis for CL. Data shown are means ±SE (n = 4). Statistical significance is indicated by * ($p < 0.05$).

(**b**) Quantitative and rate assessments of CL species by mass spectrometric analysis. A549 cells were analyzed as described in (**a**). Absolute values of selected CL species are shown as amounts of substance per cell (left panel). Relative values of selected CL species are shown as % of total CL (right panel). Data shown are means ±SE (n = 4). Statistical significance is indicated by * ($p < 0.05$), or ** ($p < 0.01$).

(**c**) The conventional CL metabolic pathway. Abbreviations: PA, phosphatidic acid; CDP-DG: cytidine diphosphate diacylglycerol; PGP, phosphatidylglycerophosphate; PG, phosphatidylglycerol; CL_N, nascent cardiolipin; CL_M, mature cardiolipin.

(**d** – **j**) Live-cell imaging of Mi-BCs and CL metabolic enzymes. EGFP-TAMM41 (**d**), EGFP-PGS1 (**e**), EGFP-PTPMT1 (**f**), EGFP-CRLS1 (**g**), EGFP-PLA2G6 (**h**), EGFP-TAZ (**i**), and EGFP-PRELI (**j**) were incorporated into Mi-BCs. Lower right: line-scan of fluorescence intensities along the dashed arrow. See also Supplementary Movie 7.

(**k**, **l**) Live-cell imaging of Mi-BCs and LONP1/PLD6. EGFP-LONP1 (**k**) and EGFP-PLD6 (**l**) were not incorporated into Mi-BCs. Lower right: line-scan of fluorescence intensities along the dashed arrow. See also Supplementary Movie 7.

Figure 6. Mieap is highly concentrated in mitochondrial BCs.

(**a**) 3D reconstruction showing the spatial relationship between Mi-BCs (TagRFP-T-Mieap) and mitochondrial inner membranes visualized with EGFP-TAMM41 in HeLa cells. See also Supplementary Movies 8 and 10.

(**b**) 3D reconstruction showing the spatial relationship between Mi-BCs (TagRFP-T-Mieap) and NAO in A549 cells. See also Supplementary Movies 9 and 10.

(**c** – **e**) 3D reconstruction showing the spatial relationship between BCs formed by TagRFP-T-Mieap ΔCC (**c**), Δ275 (**d**), and Δ496 (**e**) and mitochondrial inner membranes visualized with EGFP-TAMM41 in HeLa cells. See also Supplementary Movies 8 and 10.

(**f** – **h**) 3D reconstruction showing the spatial relationship between BCs formed by TagRFP-T-Mieap ΔCC (**f**), Δ275 (**g**), and Δ496 (**h**) and NAO in A549 cells. See also Supplementary Movies 9 and 10.

(**i**) The intensity ratio (IR) of EGFP-Mieap WT, ΔCC, Δ275, or Δ496 protein in condensates and cytoplasm, displayed in violin plot. n = 40 cells for each construct in A549 cells. Statistical significance is indicated by ** ($p < 0.01$), *** ($p < 0.001$), or **** ($p < 0.0001$). When the data were visualized using violin plots, box plots were overlaid. The center line in the box indicates the median. The bottom and top of the box indicate the 25th and 75th percentiles. The whiskers extend 1.5 times the interquartile range (IQR) from the top and bottom of the box unless the minimum and maximum values are within the IQR. The values which fall above or below the whiskers are plotted individually as outliers.

Figure 7. Both N- and C-terminal regions of Mieap are required to phase separate CL metabolic enzymes by generating the multi-phase structure of Mi-BCs.

(**a** – **d**) Comparison of phase-separating behaviors on the CL metabolic enzyme, TAMM41 (EGFP-TAMM41), between BCs formed by TagRFP-T-Mieap WT (**a**), ΔCC (**b**), Δ275 (**c**), and Δ496 (**d**) in HeLa cells. Right: line-scan of fluorescence intensities along the dashed arrow.

(**e** –**h**) CL metabolic enzymes wet the interface in the Mieap-depleted phase of Mi-BCs. Distributions of the CL metabolic enzymes, EGFP-PGS1 (**e**, **f**) and EGFP-TAMM41 (**g**, **h**), in the Mieap-depleted phase of Mi-BCs are shown in HeLa cells. Lower right: line-scan of fluorescence intensities along the dashed arrow.

(**i** – **l**) CL metabolic enzymes wet the interface in the Mieap Δ496-depleted phase of Δ496-BCs. Distributions of the CL metabolic enzymes, EGFP-PGS1 (**i**, **j**) and EGFP-TAMM41 (**k**, **l**), in the Mieap Δ496-depleted phase of BCs formed by the Δ496 mutant are shown in HeLa cells. Lower right: line-scan as in (**e** – **h**).

Figure 8. Mieap may promote mitochondrial quality control by regulating CL metabolism.

(**a**) Oxygen consumption rates (OCR) of LS174T-cont and Mieap-KD cells under normal conditions calculated with a flux analyzer. Data are shown as means ± SD (n = 9).
(**b**) Mitochondrial ATP production rates of LS174T-cont and Mieap-KD cells under normal conditions calculated with a flux analyzer, using a Seahorse XF real-time ATP rate assay. Data are shown as means ± SD (n = 9).
(**c**) Morphology of mitochondria of LS174T-cont and Mieap-KD cells with transmission electron microscopy (TEM).
(**d**) Ratio of crista area per mitochondrial section of LS174T-cont and Mieap-KD cells. Quantitative data were obtained from cont mitochondria (n=197) and Mieap-KD mitochondria (n= 329) in TEM images and displayed in a violin plot.
(**e**) Quantitative assessment of total CL by mass spectrometric analysis. LS174T cells with (Cont) and without (Mieap-KD) endogenous Mieap expression were subjected to mass spectrometric analysis. Data shown are means ± SE (n = 6).
(**f**) Quantitative and rate assessments of CL species by mass spectrometric analysis. LS174T cells were analyzed as described in (**e**). Absolute values of selected CL species are shown as the amount of substance per cell (left panel). Relative values of selected CL species are shown as % of total CL (right panel). Data shown are means ± SE (n = 6). See also Supplementary Data 1.
(**g**) The kinetic profile of the OCR using the Seahorse XF Real-Time ATP rate assay in HCT116 cells infected with Ad-Mieap or Ad-empty.
(**h – j**) Quantitative assessment of OCR (**h**), mitochondrial ATP production rates (**i**), and total ATP production rates (**j**) of the HCT116 cells as in (**g**). Data are shown as means ± SD (n = 9).
(**k**) Morphology of kidney mitochondria of Mieap$^{+/+}$ and Mieap$^{-/-}$ mice with TEM.
(**l**) Ratios of crista area per mitochondrial section of Mieap$^{+/+}$ and Mieap$^{-/-}$ mouse kidneys. Quantitative data were obtained from Mieap$^{+/+}$ kidney mitochondria (n=190) and Mieap$^{-/-}$ kidney mitochondria (n= 234) in TEM images and displayed in a violin plot.
(**m**) Morphology of liver mitochondria of Mieap$^{+/+}$ and Mieap$^{-/-}$ mice with TEM.
(**n**) Ratios of crista area per mitochondrial section of Mieap$^{+/+}$ and Mieap$^{-/-}$ mouse livers. Quantitative data were obtained from Mieap$^{+/+}$ liver mitochondria (n=146) and Mieap$^{-/-}$ liver mitochondria (n= 134) in TEM images and displayed in a violin plot. (**a, b, d, e, f, h-j, l, n**) Statistical significance is indicated by * ($p < 0.05$), ** ($p < 0.01$), *** ($p < 0.001$) or **** ($p < 0.0001$). When the data were visualized using violin plots, box plots were overlaid. The center line in the box indicates the median. The bottom and top of the box indicate the 25th and 75th percentiles. The whiskers extend 1.5 times the interquartile range (IQR) from the top and bottom of the box unless the minimum and maximum values are within the IQR. The values which fall above or below the whiskers are plotted individually as outliers.

Figure 9. Mieap prevents obesity by regulating CL metabolism.

(**a**) Body weights of 1,225 Mieap$^{+/+}$, Mieap$^{+/-}$, and Mieap$^{-/-}$ mice (n = 315 Mieap$^{+/+}$, 571 Mieap$^{+/-}$, and 339 Mieap$^{-/-}$ mice, 7-130 weeks of age) were weighed. Dots and quadratic regression curves with 95% confidence intervals are shown for each genotype.
(**b** – **d**) Body weights of Mieap$^{+/+}$, Mieap$^{+/-}$, and Mieap$^{-/-}$ mice (7-130 weeks of age) (**b**), (44-104 weeks of age) (**c**), and (53-62 weeks of age) (**d**) in (**a**). Data shown are means ±SE. Statistical significance is indicated by * ($p < 0.05$), ** ($p < 0.01$), or *** ($p < 0.001$).
(**e**) Morphology of brown adipose tissue (BAT) mitochondria of Mieap$^{+/+}$ and Mieap$^{-/-}$ mice with TEM.
(**f**) The ratio of crista area per mitochondrial section of Mieap$^{+/+}$ and Mieap$^{-/-}$ mice BAT. Quantitative data were obtained from Mieap$^{+/+}$ BAT mitochondria (n=181) and Mieap$^{-/-}$ BAT mitochondria (n=129) in TEM images and displayed in a violin plot. Statistical significance is indicated by **** ($p < 0.0001$). The center line in the box indicates the median. When the data were visualized using violin plots, box plots were overlaid. The bottom and top of the box indicate the 25th and 75th percentiles. The whiskers extend 1.5 times the interquartile range (IQR) from the top and bottom of the box unless the minimum and maximum values are within the IQR. The values which fall above or below the whiskers are plotted individually as outliers.

Figure 10. Hypothetical models for Mieap-mediated sequential enzymatic reactions in CL metabolism, which facilitates mitochondrial quality control.
(**a**) Hypothetical model of biosurfactant activity of Mieap. Mieap (green) exists in the Mieap-containing phase (lipid phase) (black), as a "scaffold" protein and/or as a potential "biosurfactant." At the boundary between the surfaces of Mi-BCs (aqueous phase) and the Mieap-containing phase (lipid phase) or between the Mieap-containing phase (lipid phase) and the Mieap-depeleted phase (aqueous phase), the hydrophilic N-terminal end of Mieap always faces the aqueous phase at the boundary. (**b**, **c**) Hypothetical model for Mieap-mediated sequential enzymatic reactions in CL metabolism. Black areas indicate the Mieap-containing phase (lipid phase) containing CL and Mieap. Gray areas indicate the Mieap-depeleted (aqueous phase) containing enzymes. Sequential reactions occur at the interface between the surface of Mi-BCs (aqueous phase) and the Mieap-containing phase (lipid phase) (**b**) or between the Mieap-containing phase (lipid phase) and the Mieap-containing phase (aqueous phase) (**c**). Once Mieap (green) stably interacts with PA via its C-terminal region, one of the enzymes transiently and weakly interacts with the N-terminal region of Mieap. When Mieap interacts with TAMM41, PA is converted to CDP-DG. Such reactions between biosynthetic enzymes and corresponding substrates could be repeated until mature CL is produced. Concentration of enzymes and substrates at Mi-BC surfaces, segregation of enzymes and substrates into distinct sub-compartments of Mi-BCs, interfacial catalysis, and biosurfactant activity of Mieap may enable efficient sequential reactions for CL metabolism. Abbreviations: PA, phosphatidic acid; CDP-DG: cytidine diphosphate diacylglycerol; PGP, phosphatidylglycerophosphate; PG, phosphatidylglycerol; CLOX, oxidized cardiolipin; CLN, nascent cardiolipin; CLM, mature cardiolipin.
(**d**) A hypothetical model for mitochondrial quality control via the Mieap-MLOs-CL metabolism axis.

Figure 1

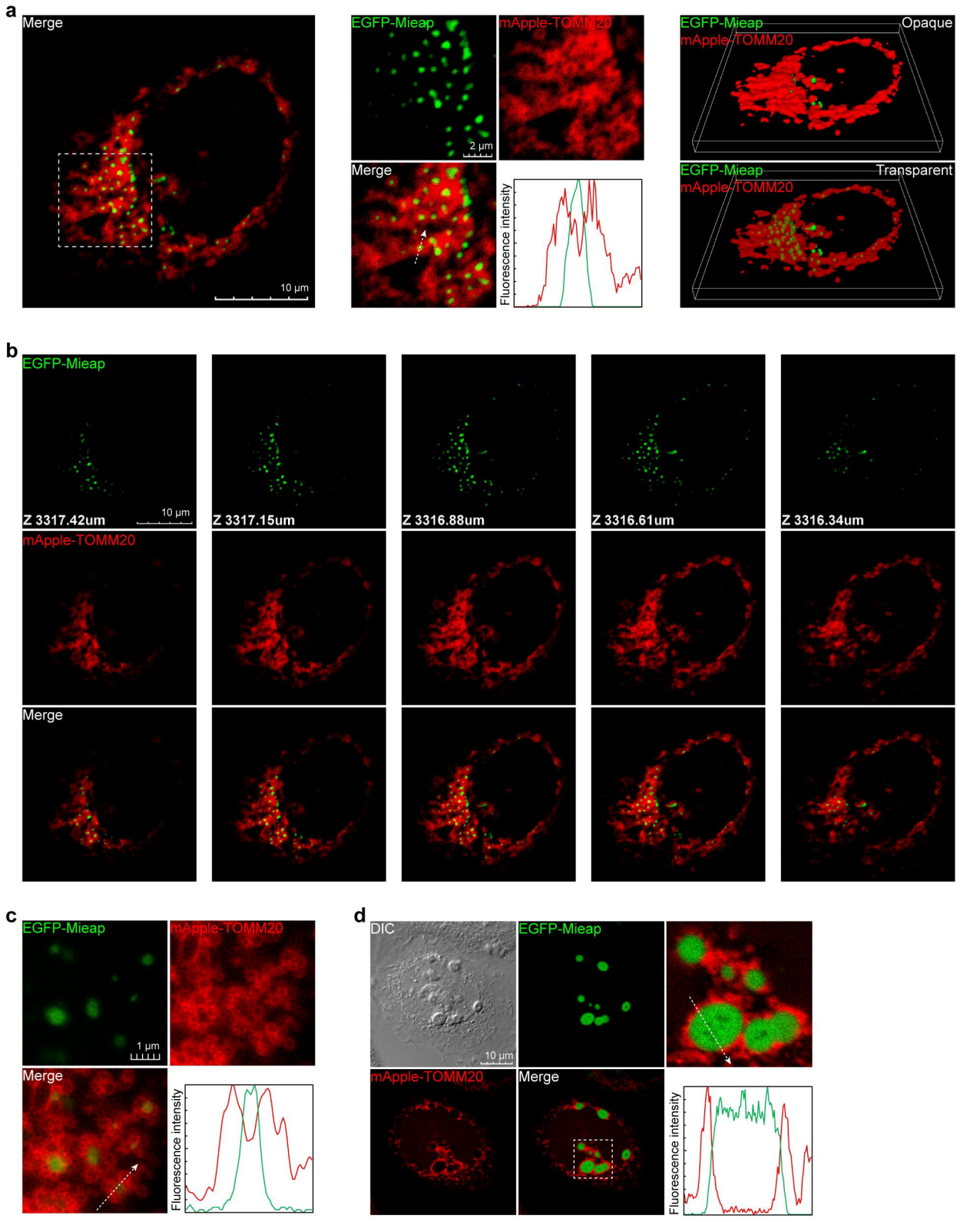
a
Merge
10 μm
EGFP-Mieap
mApple-TOMM20
2 μm
Merge
Fluorescence intensity
EGFP-Mieap
mApple-TOMM20
Opaque
EGFP-Mieap
mApple-TOMM20
Transparent
b
EGFP-Mieap
Z 3317.42um
10 μm
Z 3317.15um
Z 3316.88um
Z 3316.61um
Z 3316.34um
mApple-TOMM20
Merge
c
EGFP-Mieap
mApple-TOMM20
1 μm
Merge
Fluorescence intensity
d
DIC
10 μm
EGFP-Mieap
mApple-TOMM20
Merge
Fluorescence intensity

Figure 2

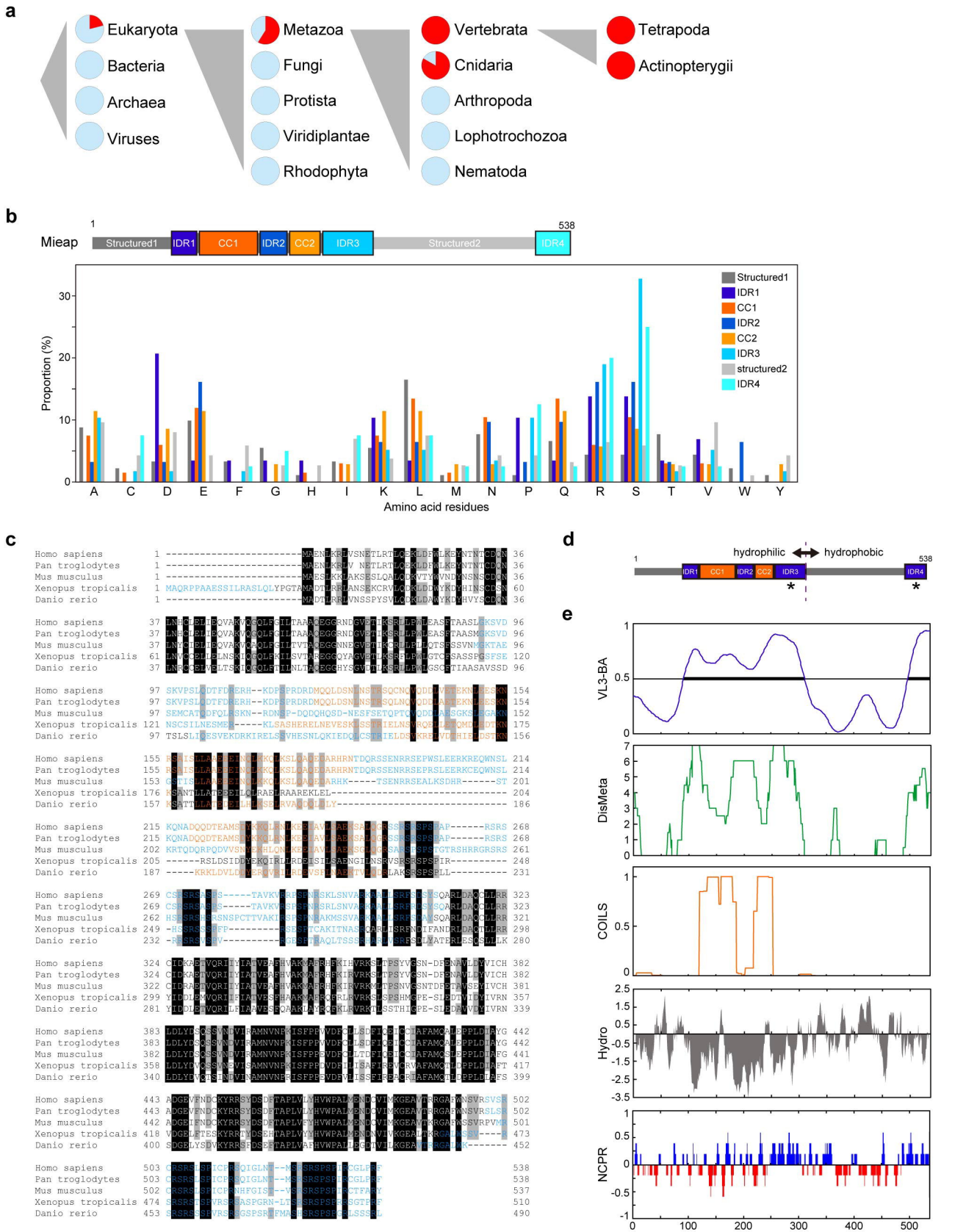
a
Eukaryota
Bacteria
Archaea
Viruses
Metazoa
Fungi
Protista
Viridiplantae
Rhodophyta
Vertebrata
Cnidaria
Arthropoda
Lophotrochozoa
Nematoda
Tetrapoda
Actinopterygii
b
Mieap
1
538
Structured1
IDR1
CC1
IDR2
CC2
IDR3
Structured2
IDR4
Proportion (%)
Amino acid residues
A C D E F G H I K L M N P Q R S T V W Y
c
Homo sapiens
Pan troglodytes
Mus musculus
Xenopus tropicalis
Danio rerio
d
hydrophilic
hydrophobic
e
VL3-BA
DisMeta
COILS
Hydro
NCPR

Figure 3

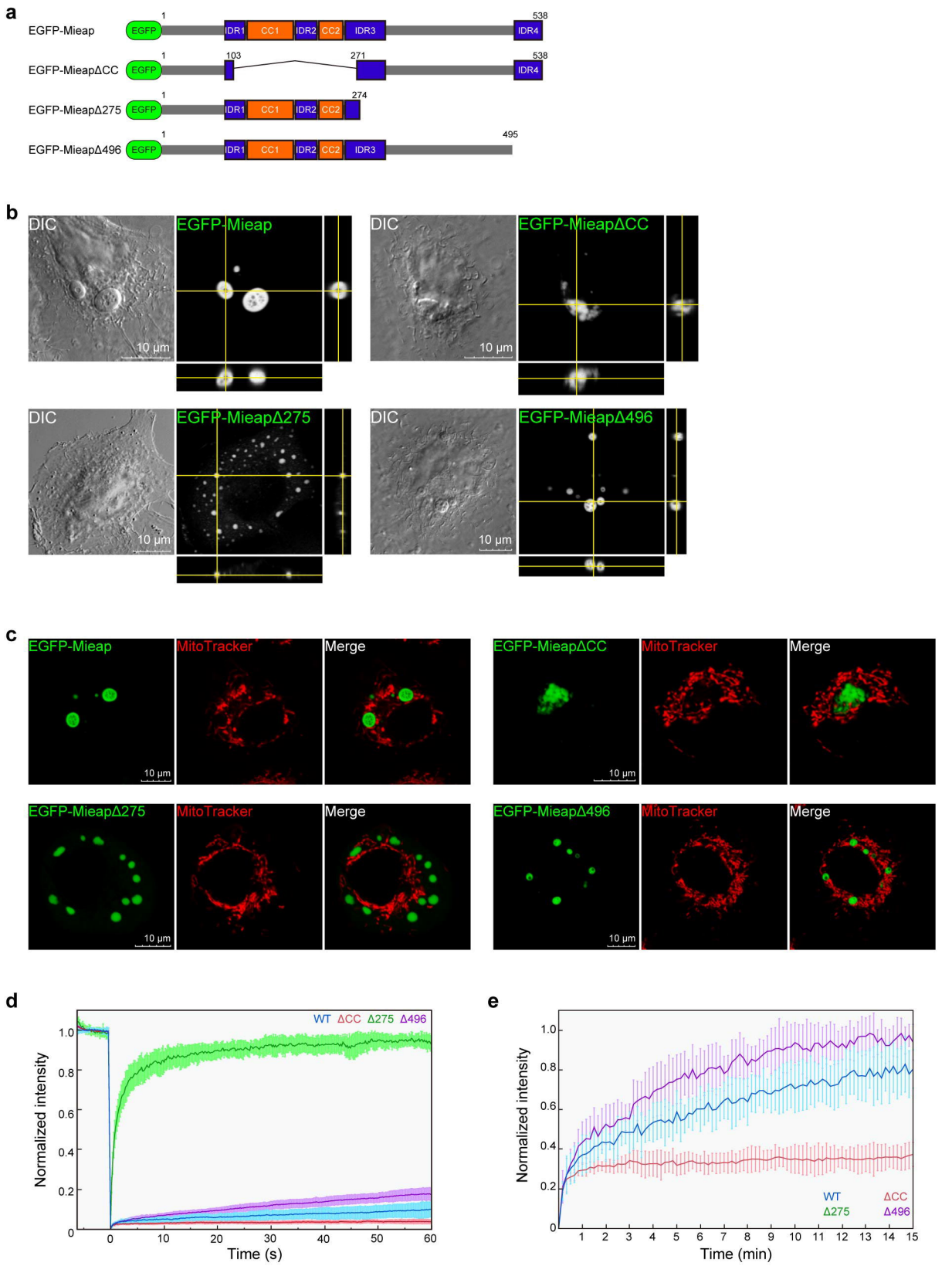
a
EGFP-Mieap
EGFP-MieapΔCC
EGFP-MieapΔ275
EGFP-MieapΔ496
EGFP
IDR1
CC1
IDR2
CC2
IDR3
IDR4
1
538
103
271
274
495
b
DIC
EGFP-Mieap
EGFP-MieapΔCC
EGFP-MieapΔ275
EGFP-MieapΔ496
10 μm
c
EGFP-Mieap
MitoTracker
Merge
EGFP-MieapΔCC
EGFP-MieapΔ275
EGFP-MieapΔ496
10 μm
d
WT ΔCC Δ275 Δ496
Normalized intensity
Time (s)
e
WT
ΔCC
Δ275
Δ496
Normalized intensity
Time (min)

Figure 4

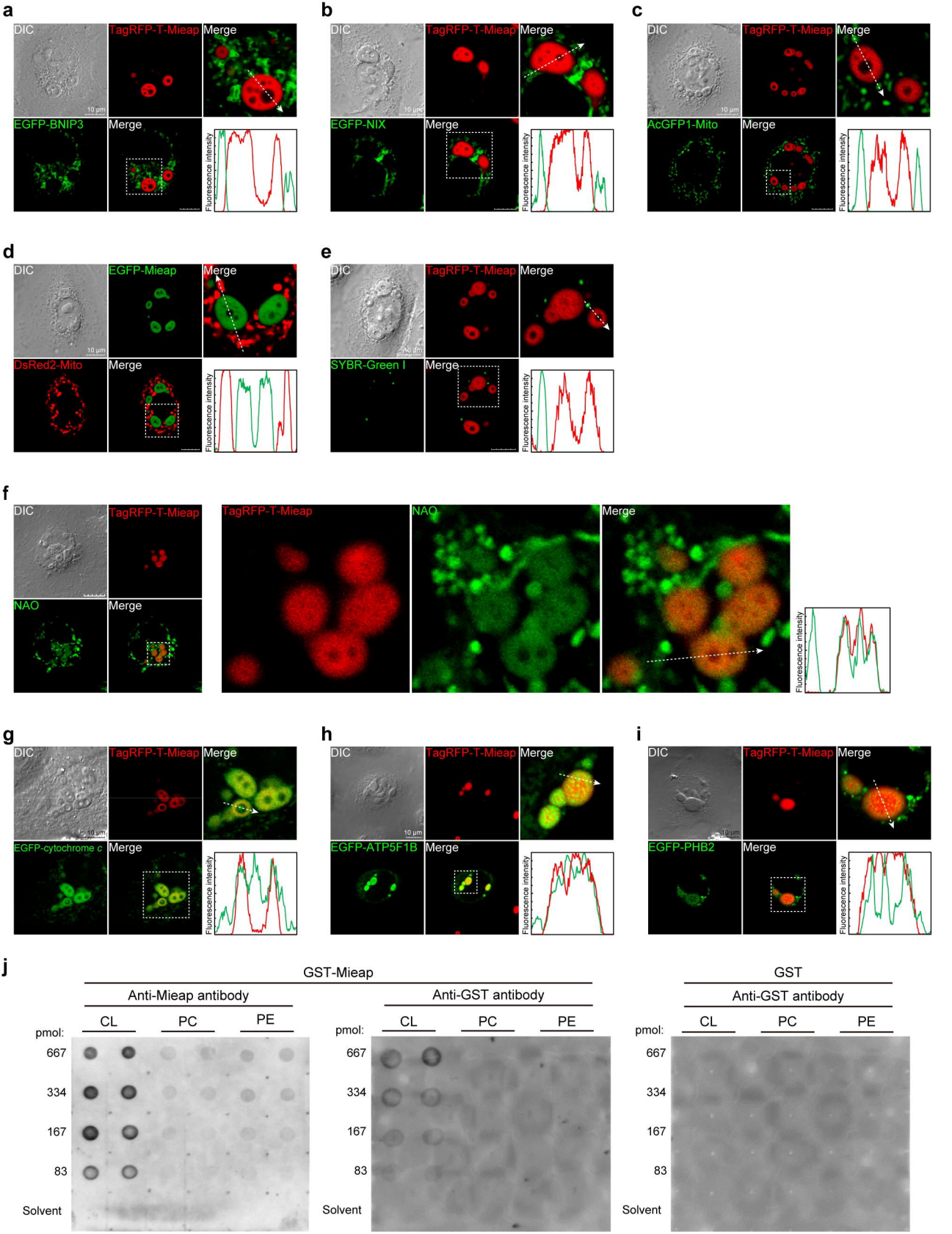
a
DIC
TagRFP-T-Mieap
Merge
EGFP-BNIP3
Merge
Fluorescence intensity
b
DIC
TagRFP-T-Mieap
Merge
EGFP-NIX
Merge
Fluorescence intensity
c
DIC
TagRFP-T-Mieap
Merge
AcGFP1-Mito
Merge
Fluorescence intensity
d
DIC
EGFP-Mieap
Merge
DsRed2-Mito
Merge
Fluorescence intensity
e
DIC
TagRFP-T-Mieap
Merge
SYBR-Green I
Merge
Fluorescence intensity
f
DIC
TagRFP-T-Mieap
NAO
Merge
TagRFP-T-Mieap
NAO
Merge
Fluorescence intensity
g
DIC
TagRFP-T-Mieap
Merge
EGFP-cytochrome c
Merge
Fluorescence intensity
h
DIC
TagRFP-T-Mieap
Merge
EGFP-ATP5F1B
Merge
Fluorescence intensity
i
DIC
TagRFP-T-Mieap
Merge
EGFP-PHB2
Merge
Fluorescence intensity
j
GST-Mieap
Anti-Mieap antibody
CL
PC
PE
pmol:
667
334
167
83
Solvent
Anti-GST antibody
CL
PC
PE
pmol:
667
334
167
83
Solvent
GST
Anti-GST antibody
CL
PC
PE
pmol:
667
334
167
83
Solvent

Figure 5

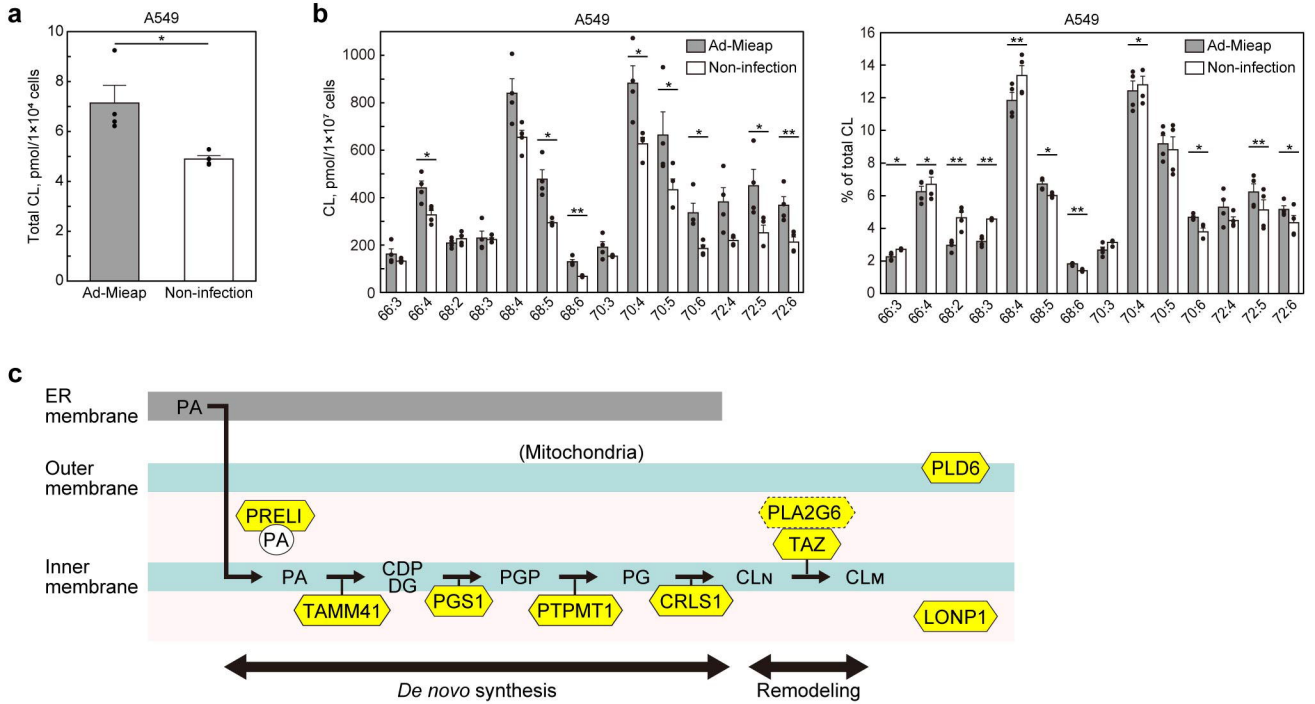
a
A549
Total CL, pmol/1×10⁴ cells
Ad-Mieap
Non-infection
b
A549
CL, pmol/1×10⁷ cells
Ad-Mieap
Non-infection
66:3
66:4
68:2
68:3
68:4
68:5
68:6
70:3
70:4
70:5
70:6
72:4
72:5
72:6
A549
% of total CL
Ad-Mieap
Non-infection
c
ER membrane
PA
(Mitochondria)
Outer membrane
PLD6
PRELI
PA
PLA2G6
TAZ
Inner membrane
PA
CDP DG
PGP
PG
CLN
CLM
TAMM41
PGS1
PTPMT1
CRLS1
LONP1
De novo synthesis
Remodeling

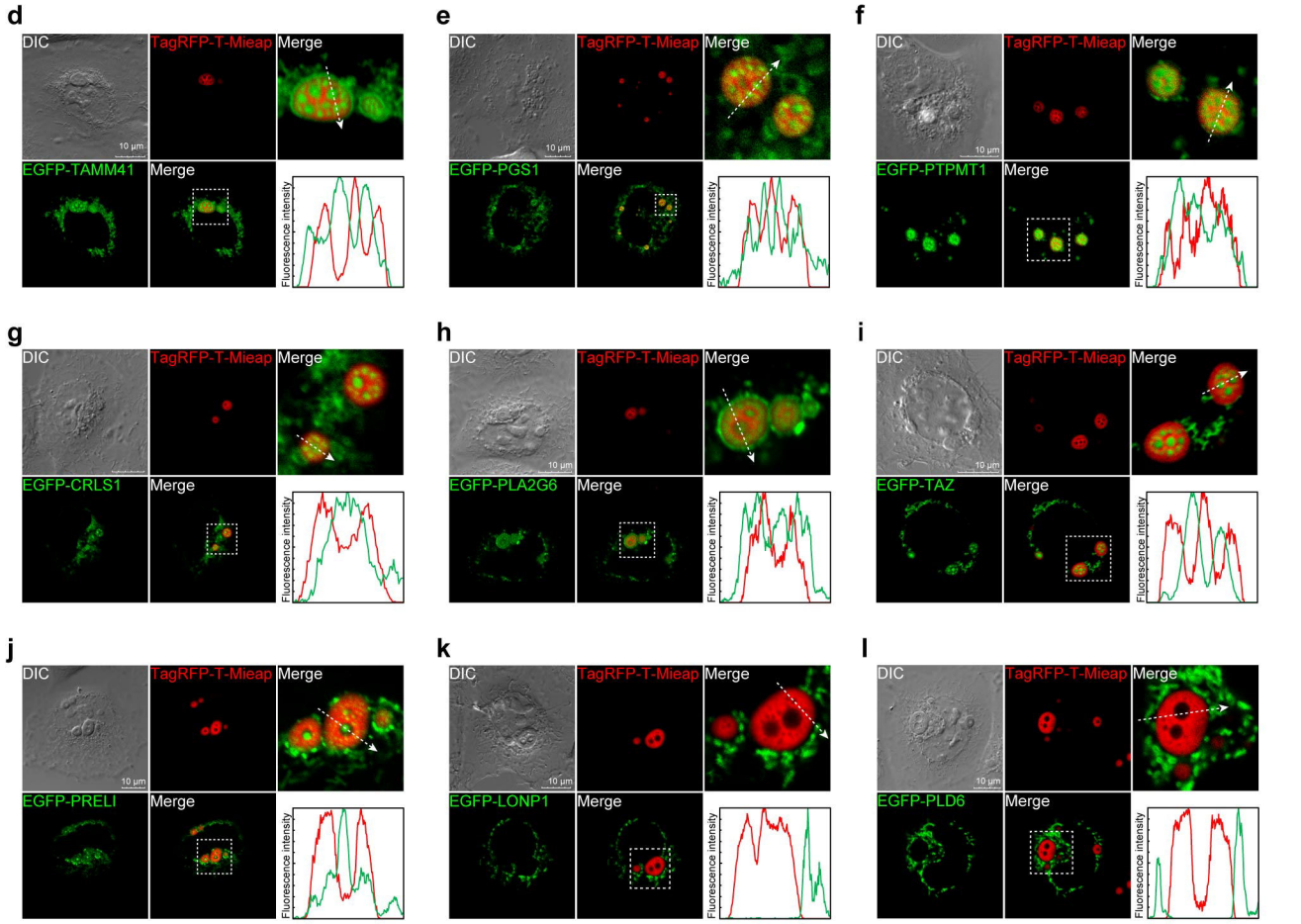
d
DIC
TagRFP-T-Mieap
Merge
10 μm
EGFP-TAMM41
Merge
Fluorescence intensity
e
DIC
TagRFP-T-Mieap
Merge
10 μm
EGFP-PGS1
Merge
Fluorescence intensity
f
DIC
TagRFP-T-Mieap
Merge
10 μm
EGFP-PTPMT1
Merge
Fluorescence intensity
g
DIC
TagRFP-T-Mieap
Merge
EGFP-CRLS1
Merge
Fluorescence intensity
h
DIC
TagRFP-T-Mieap
Merge
10 μm
EGFP-PLA2G6
Merge
Fluorescence intensity
i
DIC
TagRFP-T-Mieap
Merge
10 μm
EGFP-TAZ
Merge
Fluorescence intensity
j
DIC
TagRFP-T-Mieap
Merge
10 μm
EGFP-PRELI
Merge
Fluorescence intensity
k
DIC
TagRFP-T-Mieap
Merge
10 μm
EGFP-LONP1
Merge
Fluorescence intensity
l
DIC
TagRFP-T-Mieap
Merge
10 μm
EGFP-PLD6
Merge
Fluorescence intensity

Figure 6

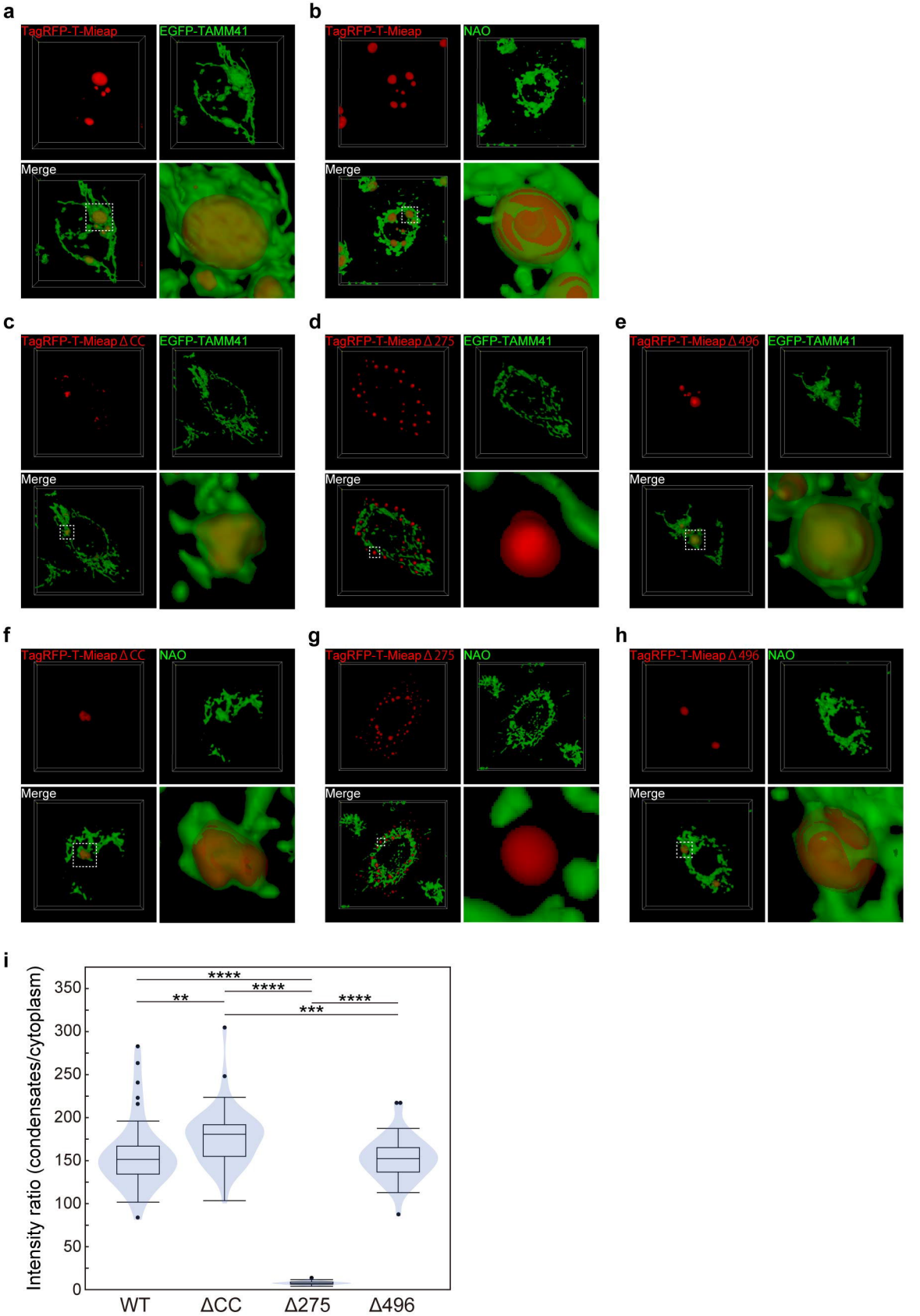
a
TagRFP-T-Mieap
EGFP-TAMM41
Merge
b
TagRFP-T-Mieap
NAO
Merge
c
TagRFP-T-Mieap Δ CC
EGFP-TAMM41
Merge
d
TagRFP-T-Mieap Δ 275
EGFP-TAMM41
Merge
e
TagRFP-T-Mieap Δ 496
EGFP-TAMM41
Merge
f
TagRFP-T-Mieap Δ CC
NAO
Merge
g
TagRFP-T-Mieap Δ 275
NAO
Merge
h
TagRFP-T-Mieap Δ 496
NAO
Merge
i
Intensity ratio (condensates/cytoplasm)
0
50
100
150
200
250
300
350
****
**
****
***
****
WT
ΔCC
Δ275
Δ496

Figure 7

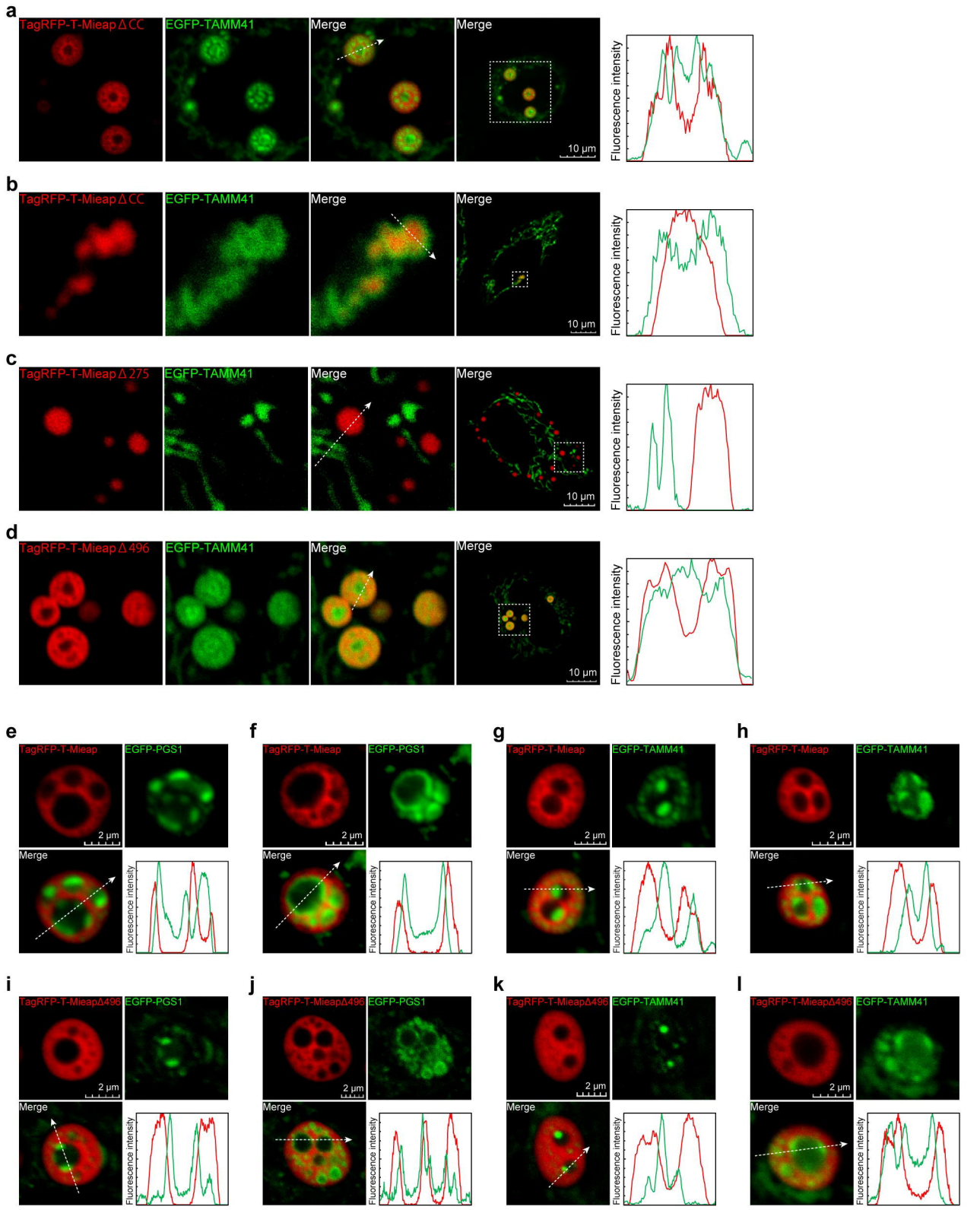
a
TagRFP-T-MieapΔCC
EGFP-TAMM41
Merge
Merge
10 μm
Fluorescence intensity
b
TagRFP-T-MieapΔCC
EGFP-TAMM41
Merge
Merge
10 μm
Fluorescence intensity
c
TagRFP-T-MieapΔ275
EGFP-TAMM41
Merge
Merge
10 μm
Fluorescence intensity
d
TagRFP-T-MieapΔ496
EGFP-TAMM41
Merge
Merge
10 μm
Fluorescence intensity
e
TagRFP-T-Mieap
EGFP-PGS1
2 μm
Merge
Fluorescence intensity
f
TagRFP-T-Mieap
EGFP-PGS1
2 μm
Merge
Fluorescence intensity
g
TagRFP-T-Mieap
EGFP-TAMM41
2 μm
Merge
Fluorescence intensity
h
TagRFP-T-Mieap
EGFP-TAMM41
2 μm
Merge
Fluorescence intensity
i
TagRFP-T-MieapΔ496
EGFP-PGS1
2 μm
Merge
Fluorescence intensity
j
TagRFP-T-MieapΔ496
EGFP-PGS1
2 μm
Merge
Fluorescence intensity
k
TagRFP-T-MieapΔ496
EGFP-TAMM41
2 μm
Merge
Fluorescence intensity
l
TagRFP-T-MieapΔ496
EGFP-TAMM41
2 μm
Merge
Fluorescence intensity

Figure 8

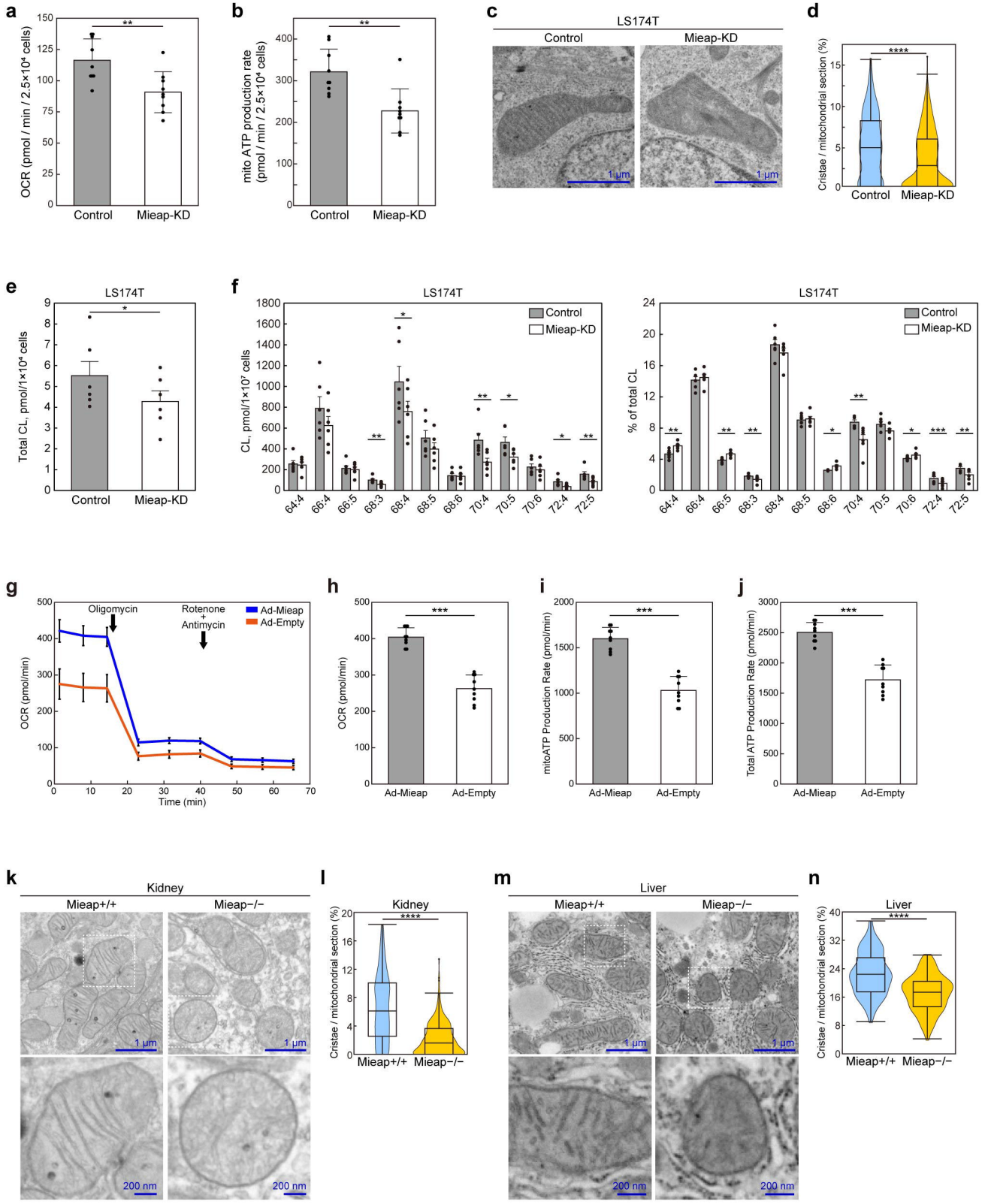
a
OCR (pmol / min / 2.5×10⁴ cells)
Control
Mieap-KD
b
mito ATP production rate (pmol / min / 2.5×10⁴ cells)
Control
Mieap-KD
c
LS174T
Control
Mieap-KD
1 μm
d
Cristae / mitochondrial section (%)
Control
Mieap-KD
e
LS174T
Total CL, pmol/1×10⁴ cells
Control
Mieap-KD
f
LS174T
CL, pmol/1×10⁷ cells
Control
Mieap-KD
64:4
66:4
66:5
68:3
68:4
68:5
68:6
70:4
70:5
70:6
72:4
72:5
LS174T
% of total CL
g
Oligomycin
Rotenone + Antimycin
Ad-Mieap
Ad-Empty
OCR (pmol/min)
Time (min)
h
OCR (pmol/min)
Ad-Mieap
Ad-Empty
i
mitoATP Production Rate (pmol/min)
Ad-Mieap
Ad-Empty
j
Total ATP Production Rate (pmol/min)
Ad-Mieap
Ad-Empty
k
Kidney
Mieap+/+
Mieap−/−
1 μm
200 nm
l
Kidney
Cristae / mitochondrial section (%)
Mieap+/+
Mieap−/−
m
Liver
Mieap+/+
Mieap−/−
1 μm
200 nm
n
Liver
Cristae / mitochondrial section (%)
Mieap+/+
Mieap−/−

Figure 9

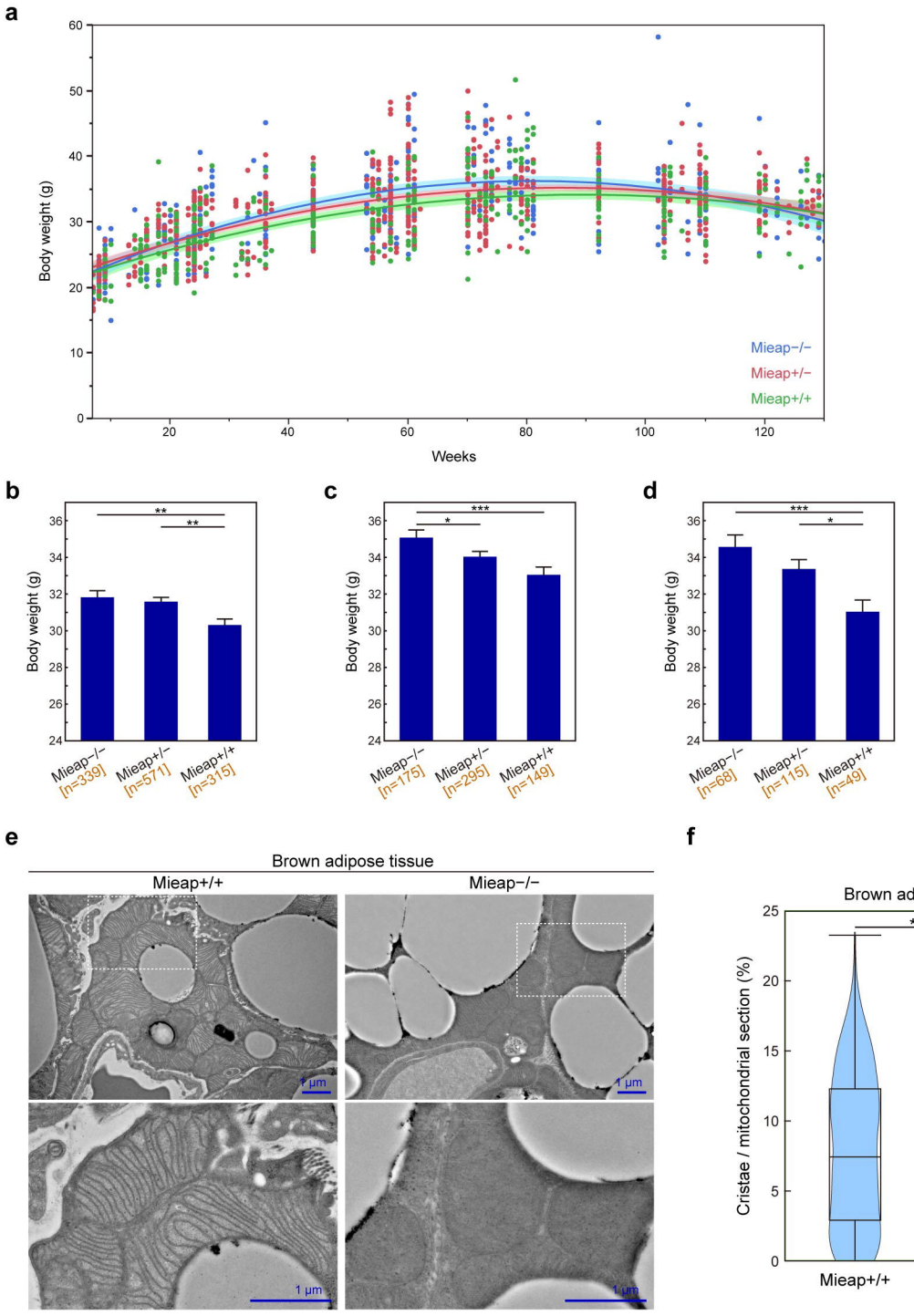
a
Body weight (g)
Weeks
Mieap−/−
Mieap+/−
Mieap+/+
b
Body weight (g)
Mieap−/− [n=339]
Mieap+/− [n=571]
Mieap+/+ [n=315]
c
Body weight (g)
Mieap−/− [n=175]
Mieap+/− [n=295]
Mieap+/+ [n=149]
d
Body weight (g)
Mieap−/− [n=68]
Mieap+/− [n=115]
Mieap+/+ [n=49]
e
Brown adipose tissue
Mieap+/+
Mieap−/−
1 μm
f
Brown adipose tissue
Cristae / mitochondrial section (%)
Mieap+/+
Mieap−/−

Figure 10

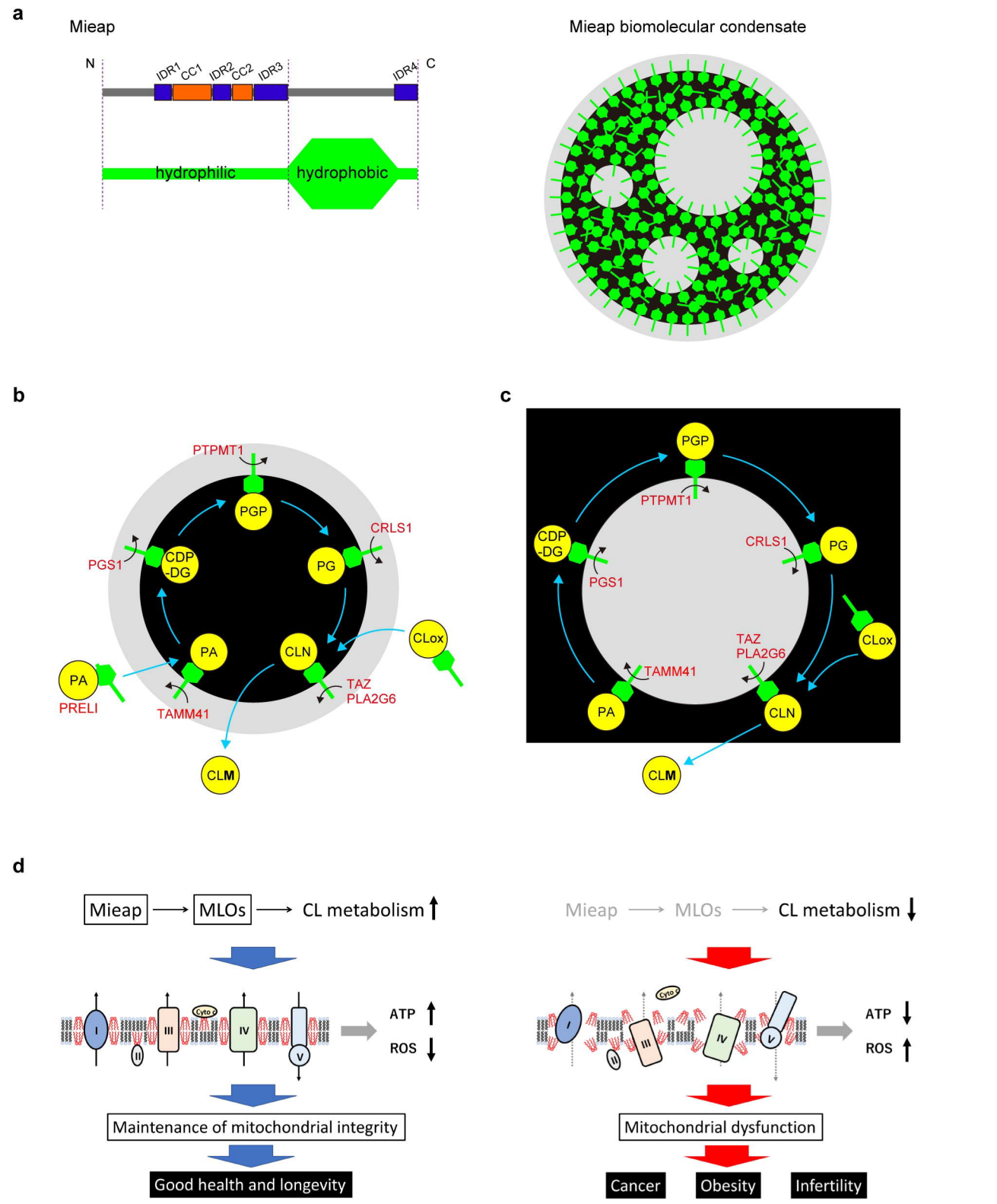
a
Mieap
N
IDR1
CC1
IDR2
CC2
IDR3
IDR4
C
hydrophilic
hydrophobic
Mieap biomolecular condensate
b
PTPMT1
PGP
CRLS1
PG
CLox
CLN
TAZ
PLA2G6
CLM
PA
TAMM41
PRELI
PGS1
CDP
-DG
c
PGP
PTPMT1
CRLS1
PG
CLox
TAZ
PLA2G6
CLN
CLM
TAMM41
PA
PGS1
CDP
-DG
d
Mieap
MLOs
CL metabolism
ATP
ROS
Cyto c
Maintenance of mitochondrial integrity
Good health and longevity
Mieap
MLOs
CL metabolism
ATP
ROS
Cyto c
Mitochondrial dysfunction
Cancer
Obesity
Infertility